1
2 **A small S-MIF signal in Martian regolith pyrite: Implications for the atmosphere**
3
4
5
6
7 Andrew G. Tomkins[1], Sarah L. Alkemade[1], Sophie E. Nutku[1], Natasha R. Stephen[2], Melanie
8 A. Finch[1], and Heejin Jeon[3]
9
10
11
12 1. School of Earth, Atmosphere and Environment, Monash University, Melbourne, Victoria

13 3800, Australia

14 2. Plymouth Electron Microscopy Centre, University of Plymouth, Drake Circus, Plymouth,

15 Devon, PL4 8AA, United Kingdom

16 3. Centre for Microscopy, Characterisation and Analysis, University of Western Australia, 35

17 Stirling Highway, Perth, Western Australia 6009, Australia

18

19

20

21 *Corresponding Author Details:

22 Andrew Tomkins

23 Email: andy.tomkins@monash.edu

24 Phone: +61 3 9905 1643

25 Fax: +61 3 9905 4903

26

28
29
30

31 **Abstract**
32
33 The past Martian atmosphere is often compared to the Archean Earth's as both were
34 dominated by CO_2-rich and O_2-poor chemistries. Archean Earth rocks preserve mass-
35 independently fractionated sulfur isotopes (S-MIF; non-zero $\Delta^{33}S$ and $\Delta^{36}S$), originating from
36 photochemistry in an anoxic atmosphere. Thus, Martian crustal rocks might also be expected
37 to preserve a S-MIF signature, providing insights into past atmospheric chemistry. We have
38 used secondary ion mass spectrometry (SIMS) to investigate in situ, the sulfur isotope
39 systematics of NWA 8171 (paired to NWA 7034), a Martian polymict breccia containing
40 pyrite that formed through hydrothermal sulfur addition in a near-surface regolith setting. In
41 this meteorite, pyrite grains have a weighted mean of $\Delta^{33}S$ of -0.14 ± 0.08 ‰ and $\Delta^{36}S$ = -
42 0.70 ± 0.40 ‰ (2 s.e.m.), so the S-MIF signature is subtle. Sulfur isotope data for four
43 additional shergottites yield $\Delta^{33}S$ values that are not resolvable from zero, as in previous
44 studies of shergottites. At first glance the result for the polymict breccia might seem
45 surprising, but no Martian meteorite yet has yielded a S-MIF signature akin to the large
46 deviations seen on Earth. We suggest that S-MIF-bearing aerosols (H_2SO_4 and S_8) were
47 produced when volcanic activity pushed a typically oxidising Martian atmosphere into a
48 reduced state. After rain-out of these aerosols, S_8 would tend to be oxidised by chlorate,
49 dampening the S-MIF signal, which might be somewhat retained in the more abundant
50 photolytic sulfate. Then in the regolith, mixing of aqueous surface-derived sulfate with
51 igneous sulfide (the latter with zero MIF), to form the abundant pyrite seen in NWA 8171,
52 would further dampen the S-MIF signal. Nonetheless, the small negative $\Delta^{33}S$ anomalies seen
53 in Martian meteorites imply that volcanic activity was sufficient to produce a reducing
54 atmosphere at times. This volcanically-driven atmospheric evolution would tend to produce
55 high levels of carbonyl sulfide (OCS). Given that OCS is a relatively long-lived strong
56 greenhouse gas, the S-MIF signal implies that volcanism periodically generated warmer
57 conditions, perhaps offering an evidence-based solution to the young wet Mars paradox.
58
59
60
61 **1. INTRODUCTION**
62
63 Geological evidence indicates that early in its history, during the late Noachian, the
64 Hesperian and into the early Amazonian (~4.0 – 2.8 Ga), Mars was likely warm with a
65 thicker atmosphere, rivers, lakes and glaciers, a groundwater system, and possibly a northern
66 ocean (cf. Hynek, 2016; Wordsworth, 2016; Kite, 2019; Lasue et al., 2019). Consequently,
67 many have suggested that the climate of Mars may have been suitable for life at this time
68 (e.g., Bibring et al., 2006; Michalski et al., 2017; Wordsworth, 2016), possibly analogous to
69 the early Earth (Michalski et al., 2017). However, this young wet Mars is yet to be achieved
70 by climate models (Kite, 2019), presenting a considerable paradox. Earth's atmosphere
71 evolved from initially very low O_2 concentrations (<10^6 x Present Earth Atmospheric Level –
72 PEAL; cf. Catling & Zahnle, 2020; Pavlov and Kasting, 2002), through at least two great
73 oxidation events (e.g., Campbell and Allen, 2008; Farquhar et al., 2014), probably caused by
74 photosynthesising microorganisms (e.g., Campbell and Squire, 2010). The first great
75 oxidation event occurred at about 2.4-2.3 Ga, and is best evidenced by a distinct change in
76 the S isotope signature of sedimentary sulfide and sulfate minerals (Farquhar et al., 2014).
77 Prior to this first great oxidation event these minerals record distinct signatures of mass-
78 independently fractionated sulfur isotopes, whereas afterwards this signature disappears
79 completely (Farquhar et al., 2014).
80

Mass-dependently fractionated sulfur isotopes fall on mass fraction curves that closely approximate straight lines, whereby $\Delta^{33}S$ and $\Delta^{36}S$ are zero ($\Delta^{33}S = \delta^{33}S_{meas} - 0.515\delta^{34}S_{meas} = 0$; and $\Delta^{36}S = \delta^{36}S_{meas} - 1.9\delta^{34}S_{meas} = 0$; Farquhar et al., 2007a). Sulfur isotope mass independent fraction (S-MIF) is indicated by data that plot off these mass-dependent lines ($\Delta^{33}S$ and $\Delta^{36}S \neq 0$) – these are a measure of the extent that $\delta^{33}S$ and $\delta^{36}S$ has deviated from the standard mass relationship with $\delta^{34}S$. After the discovery of non-zero $\Delta^{33}S$ and $\Delta^{36}S$ in Earth's Archean sedimentary rocks (Farquhar et al., 2000a), it was determined that S-MIF can be produced in reducing atmospheres via photolysis of volcanic SO_2 by ultraviolet (UV) radiation (Catling and Zahnle, 2020; Endo et al., 2016; Farquhar et al., 2001). Once fractionated, positive and negative $\Delta^{33}S$ exit the atmosphere in separate aerosols of opposing oxidation states: S_8 with *positive* $\Delta^{33}S$ and sulfate with *negative* $\Delta^{33}S$, and the opposite applies to $\Delta^{36}S$ (cf. Pavlov and Kasting, 2002; Izon et al., 2017; S_8 is a stable aerosol in reducing atmospheres because it is a ring molecule). The sign of these fractionations is also observed in experiments (e.g., Endo et al., 2016), although the validity of these results has been questioned by Harman et al. (2018). Conceptually, if the S_8 becomes oxidised, or if the sulfate is reduced, the positive and negative S-MIF reservoirs are re-homogenised, erasing the S-MIF signature (Pavlov and Kasting, 2002). However, although it comes close, SO_2 photolysis alone cannot exactly reproduce the S-MIF trend seen in Archean Earth rocks (whereby negative $\Delta^{33}S$ linearly correlates with positive $\Delta^{36}S$ and vice versa), and a range of alternatives have been suggested. For example, it is possible that a mix of this mechanism together with SO_2 photoexcitation is responsible (Endo et al., 2016; 2019). Recently, the chain formation model (Babikov, 2017) has arisen whereby sulfur atoms derived from photolysis of SO_2 are combined in low-oxygen atmospheres into progressively larger allotropes ($S_2 \rightarrow S_3 \rightarrow S_4 \rightarrow S_8$), with elemental S_4 and S_8 having strongly *negative* $\Delta^{33}S$ and strongly positive $\Delta^{36}S$ and the reverse in the remaining gas phases. Refinement of this model by Harman et al. (2018) confirmed the negative sign of $\Delta^{33}S$ produced by the chain formation model, and these authors noted that the mass-independent fractionation is much stronger than in the SO_2 photolysis model. Whatever the mechanism, the MIF signature can be preserved in sulfide or sulfate minerals that formed with a contribution from atmospheric sulfur (e.g., Catling and Zahnle, 2020); sulfides formed entirely from mantle-derived sulfur in magmas cannot contain this signature (Labidi and Cartigny, 2016). The oxidation state of the atmosphere and the depositional environment is of particular importance to S-MIF preservation. Archean Earth sedimentary rocks tend to contain either sulfides with positive $\Delta^{33}S$, or sulfates with negative $\Delta^{33}S$ (Farquhar et al., 2000a), although when sulfides from sulfate-bearing rocks are analysed they tend to differ from sulfides in non-sulfate-bearing rocks (see data in Muller et al., 2016). Given that the Martian surface is sulfate rich, this is an important observation.

Analysis of the extent and variation of S-MIF on Mars throughout its history has potential to provide key insights into its atmospheric evolution. Mars is thought to have maintained a CO_2-dominated atmosphere throughout its history (e.g., Catling and Kasting, 2017; Haberle et al., 2017), and there is no evidence that biological processes drove extreme oxygenation of the atmosphere like on Earth, and these favour preservation of S-MIF. Furthermore, Mars has had active volcanoes, and abundant sulfates are preserved at multiple localities on the surface, indicating vigorous aqueous sulfur mobilisation on and immediately beneath the surface across a broad period of time (e.g., Gaillard et al., 2013). Thus, distinct S-MIF signatures are expected to be preserved within aqueously formed or modified near-surface rocks on Mars (Sholes et al., 2017).

130 Slightly anomalous S-MIF has been reported in seven Martian meteorites, whereas the vast
131 majority of shergottites do not have anomalous S-MIF. Very slightly positive anomalies have
132 been detected in two shergottites Northwest Africa 2990 (NWA 2990 and its pair, NWA
133 5298) and Los Angeles, and slightly negative anomalies have been reported in shergottites
134 NWA 7635 and NWA 11300, and nakhlites MIL 03346, Y000593 and Nakhla (Dottin III et
135 al., 2018; Farquhar et al., 2000b; 2007b; Franz et al., 2014; 2019; Greenwood et al., 2000).
136 These results prompted the suggestion that these igneous rocks formed from magmas that
137 may have assimilated sulfur deposited by near-surface aqueous processes (Franz et al., 2014;
138 2019). However, sulfide in Nakhla has only a subtle negative S-MIF signature (Δ^{33}S of
139 −0.09‰), whereas sulfate therein is significantly more negative (Δ^{33}S of −1.25‰; Farquhar
140 et al., 2007b), implying that minimal surface sulfate was assimilated by the magma. Franz et
141 al. (2014) also recognised that since the nakhlites underwent weak hydrothermal alteration
142 (Farquhar et al., 2000b; Udry and Day, 2018), they may have acquired their anomalous
143 signature after igneous emplacement. The nakhlites and chassignites all crystallised at ca.
144 1.34 Ga and are launch-paired, and so likely came from one place on Mars (Udry and Day,
145 2018), and NWA 7635 (paired with NWA 8159) likely formed at 2.37 ± 0.25 Ga (cf. Herd et
146 al., 2017). Thus, there are relatively few samples of the Martian surface with known ages and
147 anomalous S-MIF results (the age of NWA 11300 and possible pairs is unknown, though
148 likely young). All previous work has found that Δ^{36}S for Martian meteorites is unresolvable
149 from zero (Farquhar et al., 2000b; 2007b; Franz et al., 2014; 2019). Although there are
150 effectively few sample points, the observed variation in Δ^{33}S and not Δ^{36}S has been suggested
151 to indicate that Martian atmospheric chemistry was different from that of the Archean Earth
152 (Farquhar et al., 2007b). Figure 1 shows the existing Δ^{33}S data as a function of time from
153 Martian meteorites. The shergottites are here considered unlikely to have assimilated a large
154 amount of near- or at-surface sulfur (see detail in Discussion), so they are unlikely to provide
155 a sample of atmospherically modified sulfur. Therefore, because none of the previous studies
156 have been able to sample rocks that experienced extensive sulfur addition by near-surface
157 alteration, and the nakhlites and NWA 7635 only represent two points in time separated by a
158 billion years, we currently have only the vaguest idea of the past atmospheric chemistry of
159 Mars as it relates to S isotope fractionation.
160
161 In 2013, the first meteoritic sample of the Martian regolith was recovered and has since been
162 the subject of extensive research focusing on the Martian near-surface environment (Agee et
163 al., 2013; Hewins et al., 2017; see more below). NWA 7034 (and pairs: NWA 7475, 7533,
164 7906, 7907, 8114, 8171, 8674, 10922, 11220, 11522, 11896, 11921 and Rabt Sbayta 003,
165 010) is a polymict regolith breccia featuring extensive secondary alteration and abundant
166 hydrothermal sulfides from the near-surface of Mars (Humayun et al., 2013). It has been
167 suggested that high temperature lithification of the breccia occurred at around 1.35 Ga
168 (Hewins et al., 2017), although Cassata et al. (2018) found evidence for protracted heating
169 between 1.5 and 1.2 Ga. Although the ages of the hydrothermal alteration and pyrite
170 formation have not been specifically determined, the pyrite is thought to have formed at
171 ~400-500°C (cf. Lorand et al., 2018), which is hotter than the closure temperature of the
172 ^{40}Ar/^{39}Ar system employed by Cassata et al. (2018). Thus, one might surmise that these
173 formed through hydrothermal convection in a sub- or near-crater setting shortly after impact-
174 associated lithification, sometime, and perhaps repeatedly, within the 1.5-1.2 Ga window.
175 The Martian S-MIF record has not yet been updated to include this important sample. This
176 study examines the sulfur isotope abundances in hydrothermal pyrite in Martian regolith
177 breccia NWA 8171 by in-situ Secondary Ion Mass Spectrometry (SIMS). For comparison,
178 sulfides in several additional shergottites were also analysed by SIMS and traditional
179 petrographic techniques to investigate the hypothesis that the sulfides in some of these

180 formed in response to magmatic assimilation of surface sulfur. Our data are compared with
181 those published from other Martian meteorites and the Archean Earth S-MIF record to gain
182 insights into the atmospheric chemistry of Mars.
183
184
185   **2. METHODS**
186
187 Five of the shergottites examined in this study are part of the Monash University meteorite
188 collection (NWA 7320, 7397, 8656, 8716, 10170), and one, Los Angeles (BM2000, M12),
189 was previously analysed at the Natural History Museum, London, and subsequently
190 reprocessed at the University of Plymouth. We also investigated two examples of the Martian
191 polymict regolith breccia (NWA 8171 and 11220).
192
193 Reflected light microscopy was initially used to examine the petrographic and mineralogical
194 characteristics of sulfides and oxides relative to the silicate assemblage in the polymict
195 breccia and shergottites. Sulfide targets for SIMS analysis were selected based on their size
196 (>20 μm), homogeneity, and lack of fracturing.
197
198 X-Ray element maps for NWA 10170 were collected using a JEOL 7001F FEG-SEM
199 (accelerating voltage of 20 kV, 10 nA beam current, working distance of 10 mm) equipped
200 with an Oxford Instruments X-Max 50 mm2 EDS detector at Plymouth Electron Microscopy
201 Centre (PEMC), within the University of Plymouth. X-Ray element maps for Los Angeles
202 were generated using a LEO 1455VP SEM at the Imaging & Analysis Centre (IAC) at the
203 Natural History Museum London (20 kV accelerating voltage, 10 nA beam current and 8 mm
204 working distance), and subsequently reprocessed at Plymouth Electron Microscopy Centre
205 using Oxford Instruments Aztec software alongside the new NWA 10170 data.
206
207 Pyrite compositions in the regolith breccia sample NWA 8171 were investigated using a
208 JEOL JXA8500 electron probe micro-analyser (EPMA) at the Commonwealth Scientific and
209 Industrial Research Organisation (CSIRO), Victoria, Australia. EMPA analyses were
210 conducted using an acceleration voltage of 20 kV, a 10 nA beam current, defocused 5 μm
211 spots, and peak counting times of 20 seconds. Analyses were calibrated using natural and
212 synthetic mineral standards measured at the beginning of the session. The EMPA was also
213 used to collect element maps of selected areas in NWA 8171 and NWA 11220. A 8.19 x 6.14
214 mm area of NWA 8171 was mapped for element abundance at 2 μm resolution operating at
215 15.0 kV acceleration voltage, beam current 100 nA and dwell time of 20 s per pixel. A 2.60 x
216 2.35 mm area covering an impact melt spherule in NWA 11220 was mapped for element
217 abundance at 1 μm resolution operating at 15.0 kV acceleration voltage, beam current 100 nA
218 and dwell time of 20 s per pixel. Synthetic standards were used for instrument calibration
219 prior to mapping. Data analysis of both scans, using cluster routines via a CSIRO-developed
220 program, CHIMAGE, was conducted to produce mineral phase maps. These mineral phase
221 maps were quantified with spot analyses on representative selections of pyroxene, feldspar,
222 sulfides and minor phases. Major and minor element analyses of pyroxene, feldspar, apatite
223 and minor phases were conducted at 15.0 kV and beam current of 20 nA with a defocused
224 beam size of 5 μm. Major and minor element analysis of pyrite was conducted at 15.0 kV
225 acceleration voltage and beam current of 100 nA with dwell times of 20 s for Fe and S, and
226 60 s for As, Co and Ni with a defocused beam size of 1 μm.
227
228
229 **2.1. Secondary Ion Mass Spectrometry analysis**

Secondary-Ion Mass Spectrometry (SIMS) was used to investigate four sulfur isotopes (^{32}S, ^{33}S, ^{34}S and ^{36}S) in individual sulfide mineral grains in NWA 8171 (polymict breccia), NWA 7320, NWA 7397, NWA 8656, and NWA 8716, allowing the textural relationship between sulfides and the associated silicates and oxides to be retained. The analysis was performed on the CAMECA IMS-1280 ion microprobe at the Centre for Microscopy, Characterisation and Analysis at the University of Western Australia. Prior to analysis, samples were cleaned with ethanol, and coated with 30 nm of gold to ensure conductivity across the sample surface. Previously identified sulfide grains were grouped by size (>20, >10 and >7 µm), which were measured using three different primary beam conditions. A ca. 3 nA (Gaussian) Cs$^+$ primary ion beam operating at impact energy of 20 kV was used for the >20 and >10 µm grains, with 20 and 10 µm raster employed, and 0.8 nA for the >7 µm grains, with 5 um raster (creating 20, 10 and 7 µm craters for analysis, respectively). During analysis, removal of the gold coating around the analysis spot was ensured by 45 (3nA) or 90 s (0.8nA) pre-sputter and the secondary signals were auto-centered for the field aperture and entrance slit. Energy filtering (30 eV window and a 5 eV offset) was used and the entrance/exit slits were set to get a mass resolving power of ~5,000 m/Δm to separate hydride interferences from the S mass peak. A normal-incidence electron gun was employed to mitigate positive-charge build-up on the sample potentially caused by hitting nearby silicates. All secondary S isotopes were simultaneously collected (NMR regulated) using multicollection Faraday cups (^{32}S, ^{33}S and ^{34}S) and an electron multiplier (^{36}S). Data were collected in several cycles with 4 s integrations, where the number of analysis cycles was decided based on the secondary S intensities; 20 cycles for pyrite measurements with 3nA, and 40 cycles for pyrrhotite runs with 3nA and pyrite with 0.8nA primary beam. Matrix-matching reference materials, Sierra pyrite and Alexo pyrrhotite (reported in Laflamme et al., 2016), were measured every third analysis to correct instrumental drift and mass fractionation and determine the external reproducibility for each session as described by Laflamme et al. (2016).

Data processing and calculations were performed following standard procedure as per Farquhar et al. (2007a) and are reported in the conventional delta notation:

$$\delta^{34}S = 1000 \text{ x } (^{34}S/^{32}S)_{sample}/[(^{34}S/^{32}S)_{ref} - 1] \tag{1}$$

$$\Delta^{33}S = 1000 \text{ x } [(^{33}S/^{32}S)_{sample}/(^{33}S/^{32}S)_{ref}] - [(^{34}S/^{32}S)_{sample}/(^{34}S/^{32}S)_{ref})0.515] \tag{2}$$

$$\Delta^{36}S = 1000 \text{ x } [(^{36}S/^{32}S)_{sample}/(^{36}S/^{32}S)_{ref}] - [(^{34}S/^{32}S)_{sample}/(^{34}S/^{32}S)_{ref})1.9] \tag{3}$$

Values are reported in per mil (‰) deviation from VCDT (Vienna Canyon Diablo Troilite), as per Ding et al. (2001). The reported uncertainty of δ^xS (2σ or 95% confidence) for each sample propagates errors associated with an internal precision, drift correction, and the repeatability of the reference material. The uncertainty in Δ^{33}S is a propagation of the uncertainty in δ^{33}S and δ^{34}S using equation (3) in Laflamme et al. (2016). Following the analyses, reflected-light optical microscopy was used to assess the reliability of data by checking individual analysed spots. Data from the beam craters that crossed over onto silicates or oxidised fractures within the grain were discarded.

3. RESULTS

3.1. Sulfide Petrography of the Martian Basaltic Breccia

An extensive amount of petrography has previously been reported for the martian basaltic breccia NWA 7034 and its various parings (e.g., Gattacceca et al., 2014; Goderis et al., 2016; Hewins et al., 2017; McCubbin et al., 2016; Muttik et al., 2014; Santos et al., 2015; Wittman et al., 2015), including work focusing on the sulfide formation (Lorand et al., 2018; Lorand et al., 2015). Thus, only additional information that pertains to the currently study is included here, focusing on the sulfides.

Pyrite grains, partly oxidised on the Earth's surface, are relatively abundant in both NWA 8171 and NWA 11220, and we found broadly the same relationships reported by Lorand et al. (2018) and (Lorand et al., 2015) who studied the petrography and HSE characteristics of pyrite from NWA 7533. Important points are that: (1) some pyrite occurs as isolated euhedral to subhedral grains in breccia matrix, clasts, and impact spherules fairly evenly disseminated throughout, implying that pyrite formed late in the mineral paragenesis (Figure 2), (2) Ni-free pyrite is dominant, although some pyrite grains are Ni bearing (of 39 pyrite grains analysed by EMPA, six contained > 1 wt.% Ni and up to 3.2 wt.%; Table 1 contains representative analyses), (3) some pyrite grains occur in fine calcite veins, which cross-cut all breccia lithologies. The latter pyrite grains are thought to have formed on the fracture margins in the martian regolith, and later filled with calcite through hot desert weathering (Lorand et al., 2015).

3.2. Sulfide Petrography of the Shergottites

The sulfide assemblage in the studied shergottites is consistently pyrrhotite dominated. Individual sulfide grains contain minor pentlandite exsolution lamellae and rare chalcopyrite. Sulfide abundance generally appears to be greatest in the olivine-phyric, followed by the basaltic and poikilitic shergottites. Two sulfide populations can be distinguished in most samples: 1) polyhedral sulfide grains between silicate crystals, and 2) shock melted sub-spherical trains of sulfide grains (<10 μm) (cf. Stoffler et al., 1991). Fractured sulfides in some meteorites have been partially oxidised to Fe-oxides through terrestrial weathering.

In the four shergottites analysed for sulfur isotopes by SIMS – NWA 7320, NWA 7397, NWA 8656, and NWA 8716 – pyrrhotite grains are up to 150 μm in diameter; the sulfide grains in NWA 10170 are too small to be analysed by SIMS. In all of the examined shergottites pyrrhotite is commonly, but not exclusively, attached to Fe-Ti oxide grains (compare Figs. 3A-D), and commonly associated with the late-crystallising minerals (Figs. 3B and D). Pyrrhotite typically contains minor pentlandite and chalcopyrite exsolution lamellae (Fig. 3C).

3.3. SIMS analysis of Pyrite in Regolith Breccia NWA 8171

Twenty-two pyrite grains were analysed in situ via SIMS. After analysis, reflected light microscopy was used to rule out eight data points that were compromised by overlap with oxidised fractures within grains or adjacent silicate minerals. The 7 μm spots are not able to sample as much material as the 10 μm spots, and tend to have higher analytical errors and be more scattered (many were also ruled out due to contamination). Therefore, we focus on the results yielded by the 10 μm spots. The $\Delta^{33}S$ values for these spots range from -0.22 to -0.01 ‰ with a weighted mean $\Delta^{33}S$ of -0.14 ± 0.08 ‰ (± 2 s.e.m.), and $\delta^{34}S$ values range from -

330 5.21 to -0.70 ‰ with a weighted mean $\delta^{34}S$ of -2.1 ± 1.2‰ (± 2 s.e.m.) (Table 2, Fig. 4a).
331 Although the 2σ error bars for the individual data points (10 μm spots) overlap with the $\Delta^{33}S$
332 = 0 line in Figure 4a, the weighted mean and its error plots below the line, and we have
333 calculated 95% probability of the result being below zero. $\Delta^{36}S$ values range between -1.27 to
334 -0.13 ‰, with a weighted mean $\Delta^{36}S$ of -0.70 ± 0.40 ‰ (± 2 s.e.m.) (Table 2, Fig. 4b). Due to
335 the lower count rate of ^{36}S compared to the other S isotopes, there is a larger associated error
336 for $\Delta^{36}S$ values. Nonetheless, we calculate a 98% probability that the result is below zero.
337 Although the data overlap the Archean Earth's S-MIF field defined by a well-known
338 complimentary relationship between $\Delta^{33}S$ and $\Delta^{36}S$ (Fig. 4d), relatively few Earth samples
339 have negative anomalism in both $\Delta^{33}S$ and $\Delta^{36}S$, and no previous study has found a
340 resolvable $\Delta^{36}S$ anomaly in a Martian meteorite. The $\Delta^{33}S$ range for NWA 8171 is compared
341 with other Martian meteorites and samples from Earth in Figure 1.

343 **3.4. SIMS analysis of pyrrhotite in shergottites**

345 The sulfur-isotopic compositions of shergottites NWA 7320, 7397, 8656, 8716 are provided
346 in Table 2. None of the samples analysed in this study have a resolvable mass-independent
347 signature ($\Delta^{33}S \neq 0$) at the two-sigma level. For NWA 8656, in which 12 sulfide grains were
348 analysed, $\Delta^{33}S$ values range from -0.09 to 0.06 ‰, with a weighted mean $\Delta^{33}S$ of 0.00 ± 0.05
349 ‰ (± 2 s.e.m.), $\delta^{34}S$ values range from -1.68 to -0.40 ‰ with a weighted mean $\delta^{34}S$ of -0.89
350 ± 0.22 ‰ (± 2 s.e.m.), and $\Delta^{36}S$ values range between -0.74 to 1.45 ‰, with a weighted mean
351 $\Delta^{36}S$ of 0.32 ± 0.34 ‰ (± 2 s.e.m.). For NWA 7397, in which 8 sulfide grains were analysed,
352 $\Delta^{33}S$ values range from -0.07 to 0.11 ‰, with a weighted mean $\Delta^{33}S$ of -0.03 ± 0.03 ‰ (± 2
353 s.e.m.), $\delta^{34}S$ values range from -0.77 to 0.59 ‰ with a weighted mean of $\delta^{34}S$ of 0.02 ± 0.28
354 ‰ (± 2 s.e.m.), and $\Delta^{36}S$ values range between -1.04 to 0.30 ‰, with a weighted mean $\Delta^{36}S$
355 of -0.35 ± 0.22 ‰ (± 2 s.e.m.). We were only able to measure one sulfide grain in NWA
356 8716, and two in NWA 7320 (Table 2). For all meteorites the new data are consistent with
357 previous literature data for shergottites (Fig. 5). The pyrrhotite in our samples contains
358 submicron pentlandite exsolution lamellae that were unavoidably included in the SIMS spots,
359 empirically known to make no significant fractionation using 20 μm raster.

363 **4. DISCUSSION**

365 **4.1. Production and preservation of S-MIF on Mars**

367 Slightly negative $\Delta^{33}S$ values have been found by several authors in the paired Miller Range
368 nakhlite samples (MIL 090030, 090032, and 090036) and attributed to assimilation of surface
369 sulfate by lava flows (Dottin III et al., 2018; Franz et al., 2014; Mari et al., 2019). This
370 interpretation is supported by elevated oxidation state and rapid magnetite crystallisation seen
371 in these samples (Franz et al., 2014). Yamato 000593 also has sulfate and sulfide with
372 slightly negative $\Delta^{33}S$. The other nakhlites do not contain such clear evidence for assimilation
373 of surface sulfur, although there are a small number of anomalous $\Delta^{33}S$ values amongst the
374 near zero values reported for Nakhla (cf. Farquhar et al., 2007b; Franz et al., 2014; Mari et
375 al., 2019).

377 The slightly negative $\Delta^{33}S$ seen in the Miller Range nakhlites argue for a Martian crust
378 enriched in atmospherically modified sulfate between ~1416 and 1322 Ma (cf. Cohen et al.,
379 2017; Udry and Day, 2018). Intuitively, one might expect sulfides within the Martian regolith

breccias to at least preserve similar, if not larger, S-MIF signatures, perhaps comparable with those of the Archean Earth, because the regolith has had a prolonged residence in the Martian atmosphere-surface environment and a large amount of added sulfur. The abundant pyrite + magnetite in NWA 7034 and pairs indicates a prolonged environment of sulfur-rich and moderately reducing near-surface conditions. However, for the first time we have found that the sulfur isotope ratios of hydrothermal pyrite in a Martian regolith sample (NWA 8171), yield a $\Delta^{33}S$ value of only -0.14 ± 0.084 ‰ (2 s.e.m.). This value is less negative than some nakhlites and only slightly distinct from the shergottites (Figs. 4, 5), and is not clearly distinct from $\Delta^{33}S$ values for Earth samples younger than ~2.4 Ga, when the mechanisms for preserving S-MIF in the geologic record are considered to have been neutralised (Fig. 1).

Production and preservation of the S-MIF bearing sulfur species is dependent on several factors, as reviewed briefly in the Introduction. Our results and those of previous studies suggest that one or more factors inhibited preservation of strongly mass-independently fractionated sulfur on Mars, but allowed a subtle negative $\Delta^{33}S$ signature to be retained. Previous studies have not detected an anomalous $\Delta^{36}S$ signature, and this has been recognised as a point of difference with Earth (Franz et al., 2019), whereas we have detected a subtle negative $\Delta^{36}S$ signature. Below we explore S-MIF production and survival in two stages: 1) during S-MIF production in the atmosphere, and 2) after deposition of aerosols on the surface when the separate S-MIF reservoirs may have different preservation potential in the regolith.

4.1.1. S-MIF production in the Martian atmosphere
Photons of UV light drive photolysis of SO_2 to $SO + O$ at < 217 nm, of SO_2 to $S + O_2$ at < 208 nm, and of SO to $S + O$ at < 231 nm wavelength (Catling and Kasting, 2017). Since O_2 and O_3 absorb wavelengths shorter than ~300 nm, S-MIF cannot occur by these mechanisms in Earth's modern troposphere, although some does occur in the upper stratosphere (Whitehill et al., 2015). Pavlov and Kasting (2002) determined that S-MIF will not be preserved in an atmosphere with oxygen levels greater than 10^{-5} x PEAL (now considered to be 10^{-6} x PEAL; Catling and Zanhle, 2020). Although experiments have achieved photolysis of SO_2 at 10^{-3} x PEAL (DeWitt et al., 2010), the abundance of SO_2 used was higher than those found in nature by several factors. The weak S-MIF signature in the Martian regolith could therefore plausibly be explained by an atmosphere with oxygen levels sufficiently elevated to both limit UV transparency (and thus photolysis of SO_2) and inhibit preservation of separate S-MIF reservoirs.

Based on $^{40}Ar/^{39}Ar$ data, is has been suggested that the oxidation and sulfidation of NWA 7034 and pairs likely occurred over a protracted period from ~1500-1200 Ga (Cassata et al., 2018). Like today, Mars at this time (and since the late Hesperian) is thought to have had a thin atmosphere and thus dry climate, which allowed formation of anhydrous iron oxides like hematite at the surface (Bibring et al., 2006). Presently, the partial pressure of oxygen (pO_2) on Mars measured by the Curiosity rover is ~1.4 x 10^{-3} PEAL (Mahaffy et al., 2013). As this value is greater than 10^{-6} PEAL, it implies that S-MIF would not currently survive in Mars' atmosphere. Oxygen levels higher than 10^{-6} PEAL for the Hesperian period were recently proposed by Lanza et al. (2016) after the discovery of Mn oxides by Curiosity Rover at Gale Crater. Manganese oxides did not appear on Earth until after photosynthesis and a significant rise of O_2 levels (cf. Planavsky et al., 2014) implying that the Hesperian atmosphere on Mars was more oxidising than the present day (Lanza et al., 2016). Oxygen is primarily produced in the Martian atmosphere today by UV dissociation of CO_2 and H_2O (Barth, 1974), with the current observed ratio of 1:0.7 explained by dissociation of H_2O and preferential removal of H from the atmosphere via escape to space (Catling and Kasting, 2017). Therefore, in the

wetter past (Haberle et al., 2017), there may have been more oxygen in the atmosphere than today.

Confirming this notion, Sholes et al. (2017) found, in a study modelling the effects of volcanic emissions on the chemistry of the Martian atmosphere from 3.5 Ga to today, that oxidising conditions (with high O_2) would prevail except for periods with active volcanism, when only modest volcanic emission is required to create a reducing atmosphere. These authors found that with the introduction of volcanism, the atmosphere initially forms sulfate aerosols under oxidising conditions, driving the system into reducing conditions through oxidation of SO_2, whereupon both sulfate and S_8 aerosols could form. Whereas sulfate starts to form with minimal volcanic flux, two orders of magnitude greater flux are required before S_8 starts to form. Thus, early-formed sulfate would tend not to have a S-MIF signature, whereas the later S-bearing aerosols would. Since the lifetime of SO_2 in the atmosphere is brief (e.g., Farquhar et al., 2000b), the Martian atmosphere is likely to have switched between oxidising and reducing as a function of volcanic activity. The observations of a small negative $\Delta^{33}S$ signature in three nakhlites and the polymict breccia are consistent with some weak S-MIF development leading up to the middle Amazonian (Fig. 1), and thus support the work of Sholes et al. (2017).

The Sholes et al. (2017) models are, amongst other things, based on the estimated volcanic emissions for Mars during the Amazonian, and the proportions of gases emitted as a function of magma oxidation state and depth of emplacement, the latter derived from Gaillard et al. (2013). The proportion of the different sulfur species in volcanic gases varies as a function of pressure, with lower pressures favouring higher SO_2 production (Gaillard and Scaillet, 2009; Gaillard et al., 2011). Therefore, the balance of volcanic H_2S and SO_2 was suggested to have shifted towards greater SO_2 as the atmosphere of Mars thinned over time (Gaillard and Scaillet, 2009), and this favours generation of reducing atmospheres (Sholes et al., 2017). In the Sholes et al. (2019) model, volcanic emissions were input at ground level, whereas the largest and probably youngest volcanoes have peaks many km above this (Olympus Mons, 21.2 km; Ascraeus Mons, 18.2 km; Arsia Mons, 17.8 km; Pavonis Mons 14 km; Elysium Mons 13.8 km; Tharsis plateau, >5 km). This matters for two reasons. Firstly, much of the emissions would have occurred at lower pressure than modelled, and this favours generation of reducing atmospheres at more modest volcanic flux. Secondly, the Sholes et al. (2017) models suggest that even in reducing atmospheres, O_2 would remain relatively high (10 ppm, a mixing ratio two orders of magnitude lower than today's Martian atmosphere) above a sharp transition at ~20 km altitude (see their Fig. 4), whereas this transition height may be considerably higher given the altitude of the volcanoes. This transition height is important because it affects the extent to which UV light will be blocked and S-MIF generation inhibited (see more below).

Gaillard and Scaillet (2009) showed that there were extensive volcanic SO_2 emissions during the construction of Tharsis (probably during the late Noachian and Hesperian; Bouley et al., 2018), possibly as much as 5.4 x 10^{21} g of sulfur, with ~60% as SO_2. Before that time, the higher atmospheric pressure would have limited SO_2 emissions (Gaillard and Scaillet, 2009), and thus also generation of a reducing atmosphere (see Sholes et al., 2017). Although the atmosphere was thicker during the Hesperian, thus requiring greater volcanic input to achieve the same transition to a reducing atmosphere compared to the Amazonian (because more O_2 needs to be consumed by sulfate aerosolisation), the great magnitude of emission implies that this was the period best suited to generation of S-MIF.

An atmospheric sulfur-bearing gas that has received relatively modest attention with regards to the Archean Earth is OCS. Carbonyl sulfide is the most abundant sulfur-bearing compound in Earth's modern atmosphere despite continuous SO_2 addition from volcanoes (Krysztofiak et al, 2015) because it has a significantly longer lifetime than SO_2. OCS is a strong greenhouse gas and in Earth's current atmosphere is a precursor of sulfate aerosols that contain stratospherically generated S-MIF (Krysztofiak et al, 2015; Muller et al., 2016). Its variation in the Amazonian atmosphere of Mars was included in the Sholes et al. (2017) models. They found that with modest volcanic emissions, well within the bounds of the estimated range, OCS would build to ppm levels, concomitantly with production of H_2SO_4 and S_8 aerosols. The stability of OCS is favoured by relatively reducing conditions and elevated CO (through reactions such as $3CO + SO_2 = 2CO_2 + OCS$ [Oppenheimer et al., 2011], and $S_2 + 2CO = 2OCS$, with S and S_3 able to participate in reactions equivalent to the latter [Ueno et al., 2009; Sholes et al., 2017]). Martian magmas are more reduced than those on Earth, and so tend to produce erupted gases (Gaillard et al., 2013) that are better suited to OCS production.

It has been suggested that the S-MIF signature of Earth's Archean sulfates, can be explained by contributions to the S-MIF budget by both SO_2 and OCS photolysis (Muller et al., 2016). Ueno et al. (2009) found that at ppm level concentrations of OCS (3 ppm in their model, although the lower limit was not determined), part of the UV spectrum is shielded such that photolysis of SO_2 only occurs in the <202 nm range. Between 180 and 202 nm, SO_2 photolysis produces negative $\Delta^{33}S$, and therefore UV shielding by OCS may explain the negative signature of Archean sulfate (Ueno et al., 2009; Muller et al., 2016). However, Endo et al. (2015) found that the change in $\Delta^{33}S$ produced by OCS shielding is smaller than in the Ueno et al. (2009) model and is not required to explain the Archean Earth's isotopic record. Instead experiments show that a mix of SO_2 photolysis mechanism together with SO_2 photoexcitation can explain Earth's record (Endo et al., 2016; 2019). Given the results of Sholes et al. (2017; their figs. 3 and 4 and associated text), we suggest that the same principles should apply to the Martian atmosphere, and thus the expected sign of S-MIF raining out of the atmosphere as sulfate should be negative. Depending on the extent of volcanism, the abundance of S_8 may be one or more orders of magnitude less than the sulfate aerosol (less volcanism = larger H_2SO_4/S_8; Sholes et al., 2017). Thus, the proportion of sulfur with positive $\Delta^{33}S$ raining out onto the surface of Mars may have been low. A caveat is that the experiment-based studies of Endo et al. (2015; 2016) were generated before the chain formation model of Babikov (2017), and the latter mechanism was suggested to generate strongly negative $\Delta^{33}S$ for the S_8 aerosol. However, another potentially important observation from experiments is that photolysis of OCS, which survives for much longer in the atmosphere than SO_2, produces sulfur with both weakly negative $\Delta^{33}S$ and $\Delta^{36}S$ (Lin et al., 2011), matching our results for pyrite in the Martian regolith breccia almost exactly (Fig. 4d).

OCS is that it is a strong greenhouse gas; Ueno et al. (2009) noted that OCS at 10 ppm would have radiative forcing of ~60 W m^{-2}, about the same as that of 1% CO_2 or 100 ppm of CH_4. Thus, we suggest that the young wet Mars paradox (see e.g., Kite, 2019) might be solved by the temperature increase associated with volcanically induced increase in OCS. In Earth's modern atmosphere ozone has similar properties (see fig. 1b of Ueno et al., 2009) and its low abundance (up to 100 ppb) is sufficient to warm the stratosphere, creating an increase in temperature with altitude, which inhibits vertical mixing (warm air tends not to rise into warmer air). We suggest that the very large Martian volcanoes would have pushed SO_2 into higher levels in the atmosphere than in the Sholes et al. (2017) models – perhaps as high as 50-65 km (cf. Glaze and Baloga, 2002; Wilson and Head, 2007) – where infrared absorption

530　　by OCS would create a temperature inversion and a temporarily stable stratosphere, perhaps
531　　with a thermal profile similar to the modern Earth's. This would minimise blocking of SO_2
532　　photolysis by oxygen, allowing S-MIF to progress with minor blocking by OCS, which
533　　would tend to have negative $\Delta^{33}S$ and near zero, perhaps slightly negative $\Delta^{36}S$. After
534　　cessation of volcanism, SO_2 would disappear from the atmosphere quickly and gradually
535　　dwindling OCS would be the sole source of S-MIF for a period, before H_2O photolysis and
536　　H_2 escape returned the atmosphere to a colder, more oxidised state. This cycle likely repeated
537　　as volcanism increased and waned over time.
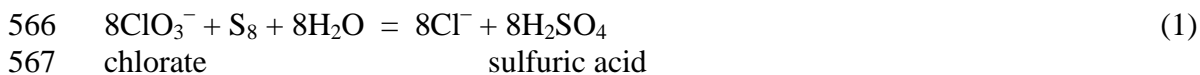538
539　　*4.1.2. Dampening of S-MIF signals in the regolith*
540　　Preservation of S-MIF in Earth's Archean rocks is thought to have required separate delivery
541　　of the photolytic products (S_8 and H_2SO_4) from the atmosphere to the surface (Pavlov and
542　　Kasting, 2002). Conceptually, if these products are not kept isolated, their negative and
543　　positive $\Delta^{33}S$ values are homogenised and the S-MIF signature can be destroyed (Pavlov and
544　　Kasting, 2002). Our near-zero $\Delta^{33}S$ value for NWA 8171 could therefore reflect mixing, and
545　　thus cancelling out, of positive and negative S-MIF reservoirs. The vast amounts of sulfate
546　　present on the surface of Mars in sedimentary deposits and in groundwater-associated
547　　bedrock cracks (Gaillard et al., 2013; Schwenzer et al., 2016) indicate that at least the
548　　oxidised sulfur species can be delivered to the surface and preserved, but elemental sulfur has
549　　not yet been observed.
550
551　　Some of the sulfate on Mars was likely produced from sulfuric acid aerosol (H_2SO_4) that
552　　rained out of the atmosphere (Gaillard et al., 2013), and this would tend to preserve negative
553　　$\Delta^{33}S$, provided that some S_8 survived without oxidation in the atmosphere. Martian soils have
554　　also been found to contain relatively abundant (per)chlorate minerals (Stern et al., 2017),
555　　which are known to be strongly deliquescent at temperatures well below 273 kelvin (Gough
556　　et al., 2011; Nuding et al., 2014; Robertson and Bish, 2011; Toner and Catling, 2018); that is,
557　　they can extract H_2O from the atmosphere and then dissolve into the liquid, which can then
558　　persist down to ~200-220 K before freezing. Chlorate is known to be a strong oxidant,
559　　whereas perchlorate is kinetically inert; both are thought to be widespread in Martian soils,
560　　and chlorate is thought to have been the primary driver of the ubiquitous Fe^{2+} oxidation there
561　　(Mitra and Catalano, 2019). Perchlorate seems to be only able to oxidise nanoscale (but not
562　　microscale) Fe metal due to extremely slow reaction kinetics (Cao et al., 2005). Thus, one
563　　might expect that elemental sulfur that mixed with soils containing chlorate with attached
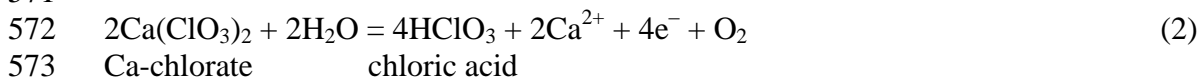564　　water might be oxidised (Fig. 6) by reactions akin to:
565
566　　$8ClO_3^- + S_8 + 8H_2O = 8Cl^- + 8H_2SO_4$　　　　　　　　　　　　(1)
567　　chlorate　　　　　　　　　　　　sulfuric acid
568
569　　This redox process may also proceed in warmer, more deeply circulating waters associated
570　　with impact events (Fig. 6), perhaps via a two-step process:
571
572　　$2Ca(ClO_3)_2 + 2H_2O = 4HClO_3 + 2Ca^{2+} + 4e^- + O_2$　　　　　　　(2)
573　　Ca-chlorate　　　　　　　chloric acid
574
575　　$8HClO_3 + S_8 + 8H_2O = 8H_2SO_4 + 8HCl$　　　　　　　　　　　(3)
576　　chloric acid　　　　　　　sulfuric & hydrochloric acid
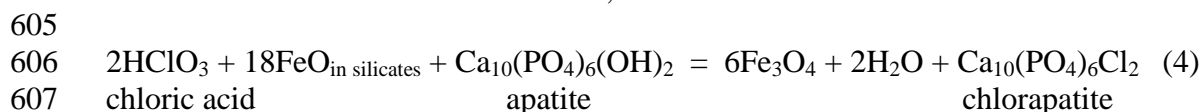577
578　　The atmospheric sulfate would have negative $\Delta^{33}S$, whereas sulfate produced via Reactions
579　　1-3 would have positive $\Delta^{33}S$, so mixing of these through formation of sulfate minerals in the
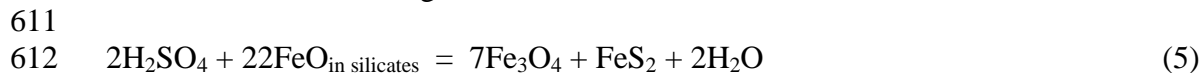
580 regolith would tend to neutralise the S-MIF signature. However, the lower proportion of S_8
581 relative to H_2SO_4 produced in the Sholes et al. (2017) models, would allow survival of a
582 weakened negative $\Delta^{33}S$ signal. The excess of chlorates in the Martian soil implies that all
583 atmospheric sulfide would be destroyed by these reactions, provided that atmospheric
584 humidity has periodically exceeded that required for (per)chlorate deliquescence; previous
585 studies have found that this is the case today (Gough et al., 2011; Nuding et al., 2014). In the
586 more distant past too, at ~1500-1200 Ma, conditions were hydrous in the deeper regolith, as
587 indicated by the mineral assemblage of NWA 7034 and pairs (Muttik et al., 2014). The large
588 range in $\delta^{34}S$ observed in Martian sediments implies that extensive processing of sulfur has
589 occurred in a wet surface environment to generate strong mass-dependent fractionation
590 (Franz et al., 2017); thus maximising the possibility of reaction between chlorates and
591 reduced sulfur.
592
593 Mapping by the Mars Odyssey Gamma Ray Spectrometer has revealed that chlorine is
594 ubiquitous on the surface of Mars, particularly at low latitudes (Keller et al., 2006), implying
595 that (per)chlorates are equivalently widespread (Carrier and Kounaves, 2015). Although we
596 do not know the extent to which (per)chlorates pervaded the Martian regolith at ~1500-1200
597 Ma, the relative lack of geologic activity during the Amazonian implies that the (per)chlorate
598 distribution was comparable to today.
599
600 NWA 7034 (and pairs) is the most oxidised Martian meteorite, containing a host of secondary
601 minerals from hydrothermal alteration (including 15 wt % magnetite; Gattacceca et al.,
602 2014), elevated hydration levels (Muttik et al., 2014), and elevated Cl (Williams et al., 2016).
603 The elevated Cl in apatite suggests that some of this oxidation may have been driven by
604 chloric acid and iron in matrix silicates, akin to:
605
606 $2HClO_3 + 18FeO_{in\ silicates} + Ca_{10}(PO_4)_6(OH)_2 = 6Fe_3O_4 + 2H_2O + Ca_{10}(PO_4)_6Cl_2$ (4)
607 chloric acid   apatite   chlorapatite
608
609 A magnetite-pyrite assemblage amongst hydrated minerals could also be formed through a
610 similar reaction involving sulfuric acid, as follows:
611
612 $2H_2SO_4 + 22FeO_{in\ silicates} = 7Fe_3O_4 + FeS_2 + 2H_2O$ (5)
613
614 This reaction can explain the lack of sulfate in NWA 7034 and pairs (Hewins et al., 2017)
615 despite the sulfate-rich surface environment of Mars, and the zero to slightly negative S-MIF
616 signature, because sulfate carries the negative S-MIF.
617
618 However, the pyrite in this meteorite was previously interpreted to have formed from impact-
619 generated, near neutral and H_2S and/or HS^- bearing hydrothermal fluids after magnetite
620 formation (Lorand et al., 2015; no mechanism for generation of the reduced sulfur species
621 was suggested). Pyrite formation involving photolytically derived reduced sulfur in fluids
622 could occur via reactions like:
623
624 $4H_2S + Fe_3O_4 = 4H_2O + FeS_2 + 2FeS$ (6)
625
626 Continued fluid interaction could then remove the FeS via:
627
628 $2H_2S + 2FeS + O_2 = 2H_2O + 2FeS_2$ (7)
629

In general, Reactions 6 and 7 could be pathways to preserve a positive Δ^{33}S signal of photolytically produced atmospheric sulfide in the Martian regolith. Although regolith pyrite produced by this mechanism may be present in some places on Mars, the slightly negative Δ^{33}S of the pyrite in NWA 7034 and pairs suggests that it cannot explain the pyrite there, and thus Reactions 4 and 5 are the preferred mechanisms.

The Lorand et al. (2015) suggestion that a near neutral H_2S-bearing fluid was involved, was based on the assumption that magmatic sulfide was not present in the breccia at the time of hydrothermal alteration. However, if pyrrhotite was present, and it is typically present in Martian mafic crust (our observation of 26 Martian meteorites), this would allow equilibration with groundwater sulfuric acid, which in turn would dampen the negative S-MIF of the sulfate towards zero (Martian magmatic sulfide has Δ^{33}S = 0.0015 ± 0.0016‰; Franz et al., 2019), consistent with the observed results:

$$4H_2SO_4 + 22FeS = 4H_2O + 3Fe_3O_4 + 13FeS_2 \qquad (8)$$
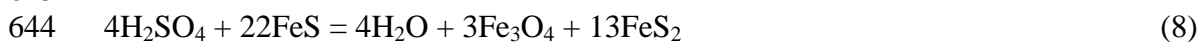
The high ratio of the zero to negative S-MIF in this reaction (22:4) implies that the dampening effect would be strong. This mechanism is also consistent with the most probable origin of S in the fluids; i.e., dissolution of the ubiquitous sulfates in the circulating groundwater, for which Schwenzer et al. (2016) provided clear evidence. The high Ni contents of some pyrite grains is also consistent with sulfidation of pentlandite-bearing pyrrhotite, which is common in shergottites. This sort of scenario is similar in some ways to the dampened S-MIF signal seen in hydrothermal volcanogenic sulfide systems in Archean Earth rocks, in which modest proportions of atmospheric S contribute to the overall budget (Jamieson et al., 2013; Chen et al., 2015). A schematic representation of the position of NWA 7034 and pairs in the context of the above discussion is shown in Figure 6.

4.2. On magmatic assimilation as a mechanism to achieve non-zero Δ^{33}S in shergottites

Only a fraction of shergottites would be capable of having a S-MIF anomaly because this can only be achieved through contamination with sulfur affected by photolysis in the atmosphere, which occurs when erupting lavas thermally erode their substrates. On Earth, this surface contamination and resulting S-MIF anomaly is seen in Archean komatiite-hosted Ni sulfide mineral deposits (Bekker et al., 2009). In these, field relationships clearly show that the extremely hot (>1600°C; Sossi and O'Neill, 2016) low viscosity, ultramafic lavas eroded through sulfidic surface materials, causing early sulfide saturation and segregation of the liquid sulfides to form ore deposits enriched in Ni, Cu and PGE (Groves et al., 1986). Basaltic shergottite lavas are not as hot and are more viscous than komatiite lavas, and would have been typically flowing over largely basaltic surfaces, so they would have lessened ability to thermally erode their substrates. Nonetheless, calculations indicate that thermal erosion is possible on Mars, and lava channels have been observed (Williams et al., 2005), indicating that mild erosion has occurred in some places. Indeed, most shergottites have Δ^{33}S within error of zero (Franz et al., 2014; 2019), including those examined here (Table 2, Fig. 5).

The four shergottites identified so far with subtly anomalous S-MIF (NWA 2990, Los Angeles, NWA 11300, and NWA 7635) were suggested to have attained their Δ^{33}S signatures by this mechanism (Franz et al., 2014; 2019). However, with the exception of NWA 7635, several factors suggest that sulfide saturation occurred late in the crystallisation history of

these basalts, implying that S addition did not occur. Firstly, the non-depleted concentrations of Ni and Co in the bulk rock in NWA 2990 and Los Angeles (no data for NWA 11300), and in olivine in NWA 2990 (Yang et al., 2015), indicate late sulfide saturation because these metals are chalcophile and thus become depleted from the magma upon sulfide saturation. Consistent with this, the sulfides in NWA 10170 (paired to 2990) and Los Angeles are commonly in association with iron-titanium oxides (Fig. 3), suggesting that considerable crystallisation occurred before sulfur saturation, which was probably achieved by loss of FeO from the silicate liquid upon oxide crystallisation (cf. O'Neill & Mavrogenes, 2002). In addition, the O isotopes for NWA 2990 and Los Angeles are not offset from the typical Martian value (Ali et al., 2016; Bunch et al., 2009), which might be expected in a surface contamination scenario, given the anomalous O isotope data of regolith breccia NWA 7034 and pairs (cf. Wittman et al., 2015). Because the Martian surface has been accumulating meteorite and micrometeorite debris for billions of years (Tomkins et al., 2019), another indicator of surface contamination might be unusually elevated HSE abundances. The regolith breccia meteorites are HSE enriched (Goderis et al., 2016), and the surface-contaminated Miller Range nakhlite samples are subtly HSE enriched (Mari et al., 2019), whereas neither Los Angeles nor NWA 2990 (and pairs) are HSE enriched (Yang et al., 2015), again suggesting minimal surface contamination. The oxidation state of Los Angeles is also not elevated (McSween Jr. and McLennan, 2014), which would be expected if it had assimilated sulfate.

Together, the various points above suggest that NWA 2990 and Los Angeles were not contaminated by surface material, and the validity of the slightly positive $\Delta^{33}S$ result is perhaps questionable (there are insufficient data for NWA 11300 currently). However, NWA 7635 contains considerably more sulfur than other shergottites, and launch-paired NWA 8159 contains no sulfides (Herd et al., 2017) and no Ni in olivine (Shearer et al., 2019), suggesting that the former might be sulfide enriched and the latter sulfide depleted, and this would be consistent with the slightly negative $\Delta^{33}S$ for NWA 7635 (Franz et al., 2019). NWA 7635 and NWA 8159 are also magnetite-rich and oxidised (cf. Lapen et al., 2017; Herd et al., 2017; Shearer et al., 2019), consistent with sulfate assimilation (see more in Shearer et al., 2019).

4.3. Insights into comparative atmospheric evolution on Mars and Earth

The earliest part of Earth's history accessed by rocks, from 3.9 to 2.4 Ga, has a continuous record of non-zero $\Delta^{33}S$, and this signature is thought to have been removed by a dramatic rise in atmospheric oxygen driven by photosynthesising microorganisms. One might therefore ask why there appears to be more oxygen on Mars, inhibiting a strong S-MIF signature, when there is no detectable sign of photosynthesising life? We know that oxygen is produced in the Martian atmosphere by photodissociation of H_2O and then loss of H to space, and this is likely to have been true in the wetter past, but this is the case for the early Earth too. The answer appears to lie not in asking why there is oxygen in the Martian atmosphere, but why there was so little in the Archean Earth's.

On Earth, the deep and extensive oceans were ferruginous during the Archean, with huge quantities of dissolved Fe^{2+} (Bekker et al., 2010). This reduced iron buffered the atmospheric composition by removing oxygen as iron oxide precipitate, which at times formed widespread banded iron formations. Biological methane formation would have a similar effect, and has been suggested as an explanation for the increase in S-MIF signal seen between 2.7 and 2.4 Ga (Zahnle et al., 2006). Photosynthesising life is thought to have arisen

at ~2.7 Ga, but the large rise in atmospheric oxygen only occurred at ~2.4 Ga after reduced iron had largely been removed from the upper oceans (Bekker et al., 2010), and methane from the atmosphere (Zahnle et al., 2006). On Mars, the only significant iron oxide accumulation is found in the spatially limited Meridiani Planum, and here it was only precipitated in association with small bodies of standing water (Christensen and Ruff, 2004; Squires et al., 2004). There is also no evidence of extensive biological methanogenesis. These observations indicate that Mars as a planet had a limited capacity to buffer atmospheric oxygen to very low levels, allowing build-up of sulfate minerals (since the late Noachian; Bibring et al., 2006), (per)chlorates and nitrates, and minimising the opportunity for development of a strong S-MIF signature.

5. CONCLUSIONS

Through SIMS analysis of pyrite in polymict breccia NWA 8171 we have presented new multiple sulfur isotope data for the Martian regolith, supplemented with new data for four additional shergottites. The polymict breccia is the most intensely sulfidised sample of all Martian meteorites, and yet has only a subtle S-MIF signature; $\Delta^{33}S$ of -0.14 ± 0.08 ‰ and $\Delta^{36}S$ = -0.70 ± 0.40 ‰ (2 s.e.m.). Given this result, and considering all sulfur isotope data for Martian meteorites, it appears that the Martian atmosphere is not a good analogue of Earth's atmosphere during the Archean eon when life is likely to have arisen. During this period on Earth there was extensive mass-independent fractionation of sulfur in an extremely oxygen deficient atmosphere, which is recorded as a strongly positive $\Delta^{33}S$ signature in sedimentary sulfides and negative $\Delta^{33}S$ signal in sulfates. By comparison Martian meteorites have, at most, a subtly negative $\Delta^{33}S$ signature and zero to slightly negative $\Delta^{36}S$, despite having had a CO_2-dominated atmosphere for billions of years.

Having explored a range of possibilities to explain the S-MIF signature on Mars, we suggest that the sulfur isotope results reflect a combination of processes. Firstly, Mars has had a long history of having water ice, and sometimes liquid water, sparsely present at the surface, including today. So, for over four billion years there has been photolysis of H_2O into H_2 and O_2 in the atmosphere, and only modest concentrations of O_2 are needed to inhibit SO_2 photolysis to produce S-MIF. Nonetheless, previous modelling (Sholes et al., 2017) suggests that relatively modest volcanism would release a gas mix sufficient to create globally reducing conditions for brief periods. The resulting atmospheric evolution produces high levels of H_2SO_4 aerosol and a lesser amount of S_8 aerosol, which would rain out, and elevated OCS gas, which persists in the atmosphere. Within the regolith environment, chlorate would act to oxidise S_8, dampening the S-MIF signal. The magnetite and pyrite seen in the polymict breccia meteorites were likely a product of oxidation of silicates by chlorate and sulfidation of magnetite and magmatic sulfides (which have zero S-MIF) by sulfuric acid, with this mixing further dampening, but not completely removing, the S-MIF carried in the sulfate.

On the Archean Earth extensive biological methane production and enormous amounts of reduced iron in the oceans ensured persistence of a low oxygen atmosphere, whereas neither of these were present on Mars. The amount of volcanism outgassing SO_2 has also historically been smaller on Mars than Earth, thus leading to weaker S-MIF production. However, the construction of Tharsis is thought to have released large amounts of SO_2 into the atmosphere, eventually producing the extensive sulfate deposits on the Martian surface. The observed small negative $\Delta^{33}S$ anomalies imply that volcanic activity was sufficient to produce a reducing atmosphere at times, with elevated levels of OCS. Given that OCS is a strong,

780 relatively long-lived greenhouse gas, the S-MIF signal implies that volcanism periodically
781 generated warmer conditions, perhaps solving the young wet Mars paradox.
782
783
784
785 **6. ACKNOWLEDGEMENTS**
786
795
796
797 **7. AUTHOR CONTRIBUTIONS**
798
799 The project was conceptualized by A.G.T., and S.L.A. and S.E.N. completed 4th year
800 research projects on NWA 8171 (S.L.A.) and the sulfide systematics of shergottites (S.E.N.)
801 under his supervision. A.G.T. adapted their work to compile the paper. N.S. assisted with the
802 petrography and edited the manuscript. M.A.F. advised on the statistics associated with the S
803 isotope data. H.J. provided technical support for the SIMS work and processed the S isotope
804 data.
805
806

8. REFERENCES

Agee, C.B., Wilson, N.V., McCubbin, F.M., Ziegler, K., Polyak, V.J., Sharp, Z.D., Asmerom, Y., Nunn, M.H., Shaheen, R., Thiemens, M.H., Steele, A., Fogel, M.L., Bowden, R., Glamoclija, M., Zhang, Z. and Elardo, S.M. (2013) Unique meteorite from early Amazonian Mars: water-rich basaltic breccia Northwest Africa 7034. *Science* **339**, 780-785.

Ali, A., Jabeen, I., Gregory, D., Verish, R. and Banerjee, N.R. (2016) New triple oxygen isotope data of bulk and separated fractions from SNC meteorites: Evidence for mantle homogeneity of Mars. *Meteorit. Planet. Sci.* **51**, 981-995.

Babikov, D. (2017) Recombination reactions as a possible mechanism of mass-independent fractionation of sulfur isotopes in the Archean atmosphere of Earth. *Proc. Nat. Acad. Sci.* **114**, 12.

Barth, C.A. (1974) The atmosphere of Mars. *Ann. Rev. Earth Planet. Sci. 2, 333-367.*

Bekker, A., Barley, M.E., Fiorentini, M.L., Rouxel, O.J., Rumble, D. and Beresford, S.W. (2009) Atmospheric sulfur in Archean komatiite-hosted nickel deposits. *Science* **326**, 1086-1089.

Bekker, A., Slack, J.F., Planavsky, N., Krapez, B., Hofmann, A., Konhauser, K.O. and Rouxel, O.J. (2010) Iron formation: The sedimentary product of a complex interplay among mantle, tectonic, and biospheric processes. *Econ. Geol.* **105**, 467-508.

Bibring, J.-P., Langevin, Y., Mustard, J.F., Poulet, F., Arvidson, R., Gendrin, A., Gondet, B., Mangold, N., Pinet, P., Forget, F. and team, t.O. (2006) Global mineralogical and aqueous Mars history derived from OMEGA/Mars Express data. *Science* **312**, 400-404.

Bouley, S., Baratoux, D., Paulien, N., Missenard, Y. and Saint-Bézar, B. (2018) The revised tectonic history of Tharsis. *Earth Planet. Sci. Lett.* **488**, 126-133.

Bunch, T.E., Irving, A.J., Wittke, J.H., Rumble III, D., Korotev, R.L., Gellissen, M. and Palme, H. (2009) Petrology and composition of Northwest Africa 2990: A new type of fine-grained, enriched, olivine-phyric shergottite, 40th Lunar and Planetary Science Conference, p. 2272.

Campbell, I.H. and Allen, C.M. (2008) Formation of supercontinents linked to increases in atmospheric oxygen. *Nature Geosci.* **1**, 554-558.

Campbell, I.H. and Squire, R.J. (2010) The mountains that triggered the late Neoproterozoic increase in oxygen: The second Great Oxidation Event. *Geochim. Cosmochim. Acta* **74**, 4187–4206.

Cao, J.S., Elliott, D. and Zhang, W.X. (2005) Perchlorate reduction by nanoscale iron particles. *J. Nanoparticle Res.* **7**, 499–506.

Carrier, B.L. and Kounaves, S.P. (2015) The origins of perchlorate in the Martian soil. *Geophys. Res. Lett.* **42**, 3739-3745.

Cassata, W.S., Cohen, B.E., Mark, D.F., Trappitsch, R., Crow, C.A., Wimpenny, J., Lee, M.R. and Smith, C.L. (2018) Chronology of martian breccia NWA 7034 and the formation of the martian crustal dichotomy. *Sci. Adv.* **4**, eaap8306.

Catling, D.C. and Kasting, J.F. (2017) Atmospheric Evolution on Inhabited and Lifeless Worlds. Cambridge University Press, Cambridge, United Kingdom. 579 p.

Catling, D.C. and Zahnle, K.J. (2020) The Archean atmosphere. *Sci. Adv.* **6**, eaax1420.

Chen, M., Campbell, I.H., Xue, Y., Tian, W., Ireland, T.R., Holden, P., Cas, R.A.F., Hayman, P.C. and Das, R. (2015) Multiple sulfur isotope analyses support a magmatic model for the volcanogenic massive sulfide deposits of the Teutonic Bore Volcanic Complex, Yilgarn Craton, Western Australia. *Econ. Geol.* **110**, 1411-1423.

855 Christensen, P.R. and Ruff, S.W. (2004) Formation of the hematite- bearing unit in
856   Meridiani Planum: Evidence for deposition in standing water. *J. Geophys. Res. – Planet.*
857   **109**, E08003.
858 Cohen, B.E., Mark, D.F., Cassata, W.S., Lee, M.R., Tomkinson, T. and Smith, C.L. (2017)
859   Taking the pulse of Mars via dating of a plume-fed volcano. *Nature Comm.* **8**, 640.
860 DeWitt, H.L., Hasenkopf, C.A., Trainer, M.G., Farmer, D.K., Jimenez, J.L., McKay, C.P.,
861   Toon, O.B. and Tolbert, M.A. (2010) The formation of sulfate and elemental sulfur
862   aerosols under varying laboratory conditions: Implications for early Earth. *Astrobiology*
863   **10**, 773-781.
864 Ding, T., Valkiers, S., Kipphardt, H., De Bièvre, P., Taylor, P.D.P., Gonfiantini, R. and
865   Krouse, R. (2001) Calibrated sulfur isotope abundance ratios of three IAEA sulfur isotope
866   reference materials and V-CDT with a reassessment of the atomic weight of sulfur.
867   *Geochim. Cosmochim. Acta* **65**, 2433-2437.
868 Dottin III, J.W., Labidi, J., Farquhar, J., Piccoli, P., Liu, M.-C. and McKeegan, K.D. (2018)
869   Evidence for oxidation at the base of the nakhlite pile by reduction of sulfate salts at the
870   time of lava emplacement. *Geochim. Cosmochim. Acta* **239**, 186-197.
871 Endo, Y., Danielache, S.O., Ueno, Y., Hattori, S., Johnson, M.S., Yoshida, N., and
872   Kjaergaard, H.G. (2015) Photoabsorption cross-section measurements of ^{32}S, ^{33}S, ^{34}S, and
873   ^{36}S sulfur dioxide from 190 to 220nm. *J. Geophys. Res. – Planet.* **120**, 2546–2557.
874 Endo, Y., Danielache, S.O. and Ueno, Y. (2019) Total pressure dependence of sulfur mass-
875   independent fractionation by SO_2 photolysis. *Geophys. Res. Lett.* **46**, 483–491.
876 Endo, Y., Ueno, Y., Aoyama, S., and Danielache, S.O. (2016). Sulfur isotope fractionation by
877   broadband UV radiation to optically thin SO_2 under reducing atmosphere. *Earth Planet.*
878   *Sci. Lett.* **453**, 9–22.
879 Farquhar, J., Bao, H. and Thiemens, M. (2000a) Atmospheric infuence of Earth's earliest
880   sulfur cycle. *Science* **289**, 756-758.
881 Farquhar, J., Johnston, D.T. and Wing, B.A. (2007a) Implications of conservation of mass
882   effects on mass-dependent isotope fractionations: Influence of network structure on sulfur
883   isotope phase space of dissimilatory sulfate reduction. *Geochim. Cosmochim. Acta* **71**,
884   5862–5875.
885 Farquhar, J., Kim, S.-T. and Masterson, A. (2007b) Implications from sulfur isotopes of the
886   Nakhla meteorite for the origin of sulfate on Mars. *Earth Planet. Sci. Lett.* **264**, 1-8.
887 Farquhar, J., Savarino, J., Airieau, S. and Thiemens, M.H. (2001) Observation of
888   wavelength- sensitive mass- independent sulfur isotope effects during SO_2 photolysis:
889   Implications for the early atmosphere. *J. Geophys. Res. – Planet.* **106**, 32829-32839.
890 Farquhar, J., Savarino, J., Jackson, T.L. and Thiemens, M.H. (2000b) Evidence of
891   atmospheric sulphur in the Martian regolith from sulphur isotopes in meteorites. *Nature*
892   **404**, 50-52.
893 Farquhar, J. and Wing, B.A. (2003) Multiple sulfur isotopes and the evolution of the
894   atmosphere. *Earth Planet. Sci. Lett.* **213**, 1-13.
895 Farquhar, J., Zerkle, A.L. and Bekker, A. (2014) Geologic and geochemical constraints on
896   Earth's early atmosphere. in: Holland, H., Turekian, K.K. (Eds.), Treatise in
897   Geochemistry, Vol. 6: The Atmosphere, pp. 91-138.
898 Franz, H.B., Kim, S.-T., Farquhar, J., Day, J.M.D., Economos, R.C., McKeegan, K.D.,
899   Schmitt, A.K., Irving, A.J., Hoek, J. and Iii, J.D. (2014) Isotopic links between
900   atmospheric chemistry and the deep sulphur cycle on Mars. *Nature* **508**, 364-368.
901 Franz, H.B., McAdam, A.C., Ming, D.W., Freissinet, C., Mahay, P.R., Eldridge, D.L.,
902   Fischer, W.W., Grotzinger, J.P., House, C.H., Hurowitz, J.A., McLennan, S.M.,
903   Schwenzer, S.P., Vaniman, D.T., Archer Jr., P.D., Atreya, S.K., Conrad, P.G., Dottin III,
904   J.W., Eigenbrode, J.L., Farley, K.A., Glavin, D.P., Johnson, S.S., Knudson, C.A., Morris,

905   R.V., Navarro-González, R., Pavlov, A.A., Plummer, R., Rampe, E.B., Stern, J.C., Steele,
906   A., Summons, R.E. and Sutter, B. (2017) Large sulfur isotope fractionations in Martian
907   sediments at Gale crater. *Nature Geosci.* **10**, 658-662.
908   Franz, H.B., Wu, N., Farquhar, J. and Irving, A.J. (2014) A new type of isotopic anomaly in
909   shergottite sulfides. *Meteorit. Planet. Sci.* **54**, 3036-3051.
910   Gaillard, F., Michalski, J., Berger, G., McLennan, S.M. and Scaillet, B. (2013) Geochemical
911   reservoirs and timing of sulfur cycling on Mars. *Space Sci. Rev.* **174**, 251–300.
912   Gaillard F., Scaillet, B. and Arndt, N.T. (2011) Atmospheric oxygenation caused by a change
913   in volcanic degassing pressure. *Nature* **478**, 229-232.
914   Gaillard, F. and Scaillet, B. (2009) The sulfur content of volcanic gases on Mars. *Earth
915   Planet. Sci. Lett.* **279**, 34-43.
916   Gattacceca, J., Rochette, P., Scorzelli, R.B., Munayco, P., Agee, C., Quesnel, Y., Cournède,
917   C. and Geissman, J. (2014) Martian meteorites and Martian magnetic anomalies: A new
918   perspective from NWA 7034. *Geophys. Res. Lett.* **41**, 4859–4864.
919   Glaze, L.S. and Baloga, S.M. (2002) Volcanic plume heights on Mars: Limits of validity for
920   convective models. *J. Geophys. Res.* **107**, E10.
921   Goderis, S., Brandon, A.D., Mayer, B. and Humayun, M. (2016) Ancient impactor
922   components preserved and reworked in martian regolith breccia Northwest Africa 7034.
923   *Geochim. Cosmochim. Acta* **191**, 203-215.
924   Gough, R.V., Chevrier, V.F., Baustian, K.J., Wise, M.E. and Tolbert, M.A. (2011)
925   Laboratory studies of perchlorate phase transitions: Support for metastable aqueous
926   perchlorate solutions on Mars. *Earth Planet. Sci. Lett.* **312**, 371-377.
927   Greenwood, J.P., Mojzsis, S.J. and Coath, C.D. (2000) Sulfur isotopic compositions of
928   individual sulfides in Martian meteorites ALH84001 and Nakhla: Implications for crust-
929   regolith exchange on Mars. *Earth Planet. Sci. Lett.* **184**, 23-35.
930   Groves, D.I., Korkiakoski, E.A., McNaughton, N.J., Lesher, C.M. and Cowden, A. (1986)
931   Thermal erosion by komatiites at Kambalda, Western Australia and the genesis of nickel
932   ores. *Nature* **319**, 136-139.
933   Haberle, R.M., Catling, D.C., Forget, F., Smith, M.D. and Zurek, R.W. (2017) The early
934   Mars climate system, in: Haberle, R.M., Clancy, R.T., Forget, F., Smith, M.D., Zurek,
935   R.W. (Eds.), The Atmosphere and Climate of Mars. Cambridge University Press,
936   Cambridge, United Kingdom, pp. 526-568.
937   Harman, C.E., Pavlovd, A.A., Babikov, D. and Kasting, J.F. (2018) Chain formation as a
938   mechanism for mass-independent fractionation of sulfur isotopes in the Archean
939   atmosphere. *Earth Planet. Sci. Lett.* **496**, 238-247.
940   Herd, C.D.K., Walton, E.L., Agee, C.B., Muttik, N., Ziegler, K., Shearer, C.K., Bell, A.S.,
941   Santos, A.R., Burger, P.V., Simon, J.I., Tappa, M.J., McCubbin, F.W., Gattacceca, J.,
942   Lagroix, F., Sanborn, M.E., Yin, Q.-Z., Cassata, W.S., Borg, L.E., Lindvall, R.E., Kruijer,
943   T.S., Brennecka, G.A., Kleine, T., Nishiizumi, K. and Caffee, M.W. (2017) The
944   Northwest Africa 8159 martian meteorite: Expanding the martian sample suite to the early
945   Amazonian. *Geochim. Cosmochim. Acta* **218**, 1–26.
946   Hewins, R.H., Zanda, B., Humayun, M., Nemchin, A., Lorand, J.-P., Pont, S., Deldicque, D.,
947   Bellucci, J.J., Beck, P., Leroux, H., Marinova, M., Remusat, L., Göpel, C., Lewin, E.,
948   Grange, M., Kennedy, A. and Whitehouse, M.J. (2017) Regolith breccia Northwest Africa
949   7533: Mineralogy and petrology with implications for early Mars. *Meteorit. Planet. Sci.*
950   **52**, 89-124.
951   Humayun, M., Nemchin, A., Zanda, B., Hewins, R.H., Grange, M., Kennedy, A., Lorand,
952   J.P., Gopel, C., Fieni, C., Pont, S. and Deldicque, D. (2013) Origin and age of the earliest
953   Martian crust from meteorite NWA7533. *Nature* **503**, 513-516.
954   Hynek, B. (2016) The great climate paradox of ancient Mars. *Geology* **44**, 879–880.

Izon, G., Zerkle, A.L., Williford, K.H., Farquhar, J., Poulton, S.W. and Claire, M.W. (2017) Bi-ological regulation of atmospheric chemistry en route to planetary oxygenation. *Proc. Natl. Acad. Sci.* **114**, E2571–E2579.

Jamieson, J.W., Wing, B.A., Farquhar, J. and Hannington, M.D. (2013) Neoarchean seawater 6 sulphate concentrations from sulphur isotopes in massive sulphide ore. *Nat. Geosci.* **6**, 61-7 64.

Keller, J.M., Boynton, W.V., Karunatillake, S., Baker, V.R., Dohm, J.M., Evans, L.G., Finch, M.J., Hahn, B.C., Hamara, D.K., Janes, D.M., Kerry, K.E., Newsom, H.E., Reedy, R.C., Sprague, A.L., Squyres, S.W., Starr, R.D., Taylor, G.J. and Williams, R.M.S. (2006) Equatorial and midlatitude distribution of chlorine measured by Mars Odyssey GRS. *J. Geophys. Res. – Planet.* **111**, E03S08.

Kite, E.S. (2019) Geologic constraints on early Mars climate. *Space Sci Rev* **215**, 10.

Krysztofiak, G., Té, Y.V., Catoire, V., Berthet, G., Toon, G.C., Jégou, F., Jeseck, P. and Robert, C. (2015) Carbonyl Sulphide (OCS) variability with latitude in the atmosphere, *Atmos.-Ocean* **53**, 89-101.

Labidi, J. and Cartigny, P. (2016) Negligible sulfur isotope fractionation during partial melting: Evidence from Garrett transform fault basalts, implications for the late-veneer and the hadean matte. *Earth Planet. Sci. Lett.* **451**, 196-207.

Laflamme, C., Martin, L., Jeon, H., Reddy, S.M., Selvaraja, V., Caruso, S., Bui, T.H., Roberts, M.P., Voute, F., Hagemann, S., Wacey, D., Littman, S., Wing, B., Fiorentini, M. and Kilburn, M.R. (2016) In situ multiple sulfur isotope analysis by SIMS of pyrite, chalcopyrite, pyrrhotite, and pentlandite to refine magmatic ore genetic models. *Chem. Geol.* **444**, 1-15.

Lanza, N.L., Wiens, R.C., Arvidson, R.E., Clark, B.C., Fischer, W.W., Gellert, R., Grotzinger, J.P., Hurowitz, J.A., Mclennan, S.M., Morris, R.V., Rice, M.S., Bell, J.F., Berger, J.A., Blaney, D.L., Bridges, N.T., Calef, F., Campbell, J.L., Clegg, S.M., Cousin, A., Edgett, K.S., Fabre, C., Fisk, M.R., Forni, O., Frydenvang, J., Hardy, K.R., Hardgrove, C., Johnson, J.R., Lasue, J., Le Mouélic, S., Malin, M.C., Mangold, N., Martìn-Torres, J., Maurice, S., Mcbride, M.J., Ming, D.W., Newsom, H.E., Ollila, A.M., Sautter , V., Schröder, S., Thompson, L.M., Treiman, A.H., Vanbommel, S., Vaniman, D.T. and Zorzano, M.-P. (2016) Oxidation of manganese in an ancient aquifer, Kimberley Formation, Gale Crater, Mars. *Geophys. Res. Lett.* **43**, 7398-7407.

Lapen, T.J., Righter, M., Andreasen, R., Irving, A.J., Satkoski, A.M., Beard, B.L., Nishiizumi, K., Jull, A.J.T. and Caffee, M.W. (2017) Two billion years of magmatism recorded from a single Mars meteorite ejection site. *Sci. Adv.* **3**, e1600922.

Lasue, J., Clifford, S.M., Conway, S.J., Mangold, N. and Butcher, F.E.G. (2019) The hydrology of Mars including a potential cryosphere, in: Filiberto, J., Schwenzer, S.P. (Eds.), Volatiles in the Martian crust. Elsevier, pp. 185-246.

Lin, Y., Sim, M.S. and Ono, S. (2011) Multiple-sulfur isotope effects during photolysis of carbonyl sulfide. *Atmos. Chem. Phys.* 11,10283–10292.

Lorand, J.P., Hewins, R.H., Humayun, M., Remusat, L., Zanda, B., La, C. and Pont, S. (2018) Chalcophile-siderophile element systematics of hydrothermal pyrite from martian regolith breccia NWA 7533. *Geochim. Cosmochim. Acta* **241**, 134-149.

Lorand, J.P., Hewins, R.H., Remusat, L., Zanda, B., Pont, S., Leroux, H., Marinova, M., Jacob, D., Humayun, M., Nemchin, A., Grange, M., Kennedy, A. and Gopel, C. (2015) Nickeliferous pyrite tracks pervasive hydrothermal alteration in Martian regolith breccia: A study in NWA 7533. *Meteorit. Planet. Sci.* **50**, 2099-2120.

Mahaffy, P.R., Webster, C.R., Atreya, S.K., Franz, H., Wong, M., Conrad, P.G., Harpold, D., Jones, J.J., Leshin, L.A., Manning, H., Owen, T., Pepin, R.O., Squyres, S. and Trainer, M.

1004   (2013) Abundance and isotopic composition of gases in the Martian atmosphere from the
1005   Curiosity Rover. *Science* **341**, 263-266.
1006 Mari, N., Riches, A.J.V., Hallis, L.J., Marrocchi, Y., Villeneuve, J., Gleissner, P., Becker, H.
1007   and Lee, M.R. (2019) Syneruptive incorporation of martian surface sulphur in the nakhlite
1008   lava flows revealed by S and Os isotopes and highly siderophile elements: Implication for
1009   mantle sources in Mars. *Geochim. Cosmochim. Acta* **266**, 416-434.
1010 McCubbin, F.M., Boyce, J.W., Novak-Szabo, T., Santos, A.R., Tartese, R., Muttik, N.,
1011   Domokos, G., Vazquez, J., Keller, L.P., Moser, D.E., Jerolmack, D.J., Shearer, C.K.,
1012   Steele, A., Elardo, S.M., Rahman, Z., Anand, M., Delhaye, T. and Agee, C. (2016)
1013   Geologic history of Martian regolith breccia Northwest Africa 7034: Evidence for
1014   hydrothermal activity and lithologic diversity in the Martian crust. *J. Geophys. Res. –
1015   Planet.* **121**, 2120-2149.
1016 McSween Jr., H.Y. and McLennan, S.M. (2014) Mars, in: Davis, A.M. (Ed.), Treatise on
1017   Geochemistry, Volume 2: Planets, Asteroids, Comets and The Solar System. Elsevier
1018   Science, pp. 250-300.
1019 Michalski, J.R., Onstott, T.C., Mojzsis, S.J., Mustard, J., Chan, Q.H.S., Niles, P.B. and
1020   Johnson, S.S. (2017) The Martian subsurface as a potential window into the origin of life.
1021   *Nature Geosci.* **11**, 21–26.
1022 Mitra, K., & Catalano, J. G. (2019). Chlorate as a potential oxidant on Mars: Rates and
1023   products of dissolved Fe(II) oxidation. *J. Geophys. Res.: Planets* **124**.
1024   https://doi.org/10.1029/2019JE006133.
1025 Muller, E., Philippota, P., Rollion-Barda, C. and Cartigny, P. (2016) Multiple sulfur-isotope
1026   signatures in Archean sulfates and their implications for the chemistry and dynamics of
1027   the early atmosphere. *Proc. Nat. Acad. Sci.* **113**, no. 27.
1028 Muttik, N., McCubbin, F.M., Keller, L.P., Santos, A.R., McCutcheon, W.A., Provencio, P.P.,
1029   Rahman, Z., Shearer, C.K., Boyce, J.W. and Agee, C.B. (2014) Inventory of H_2O in the
1030   ancient Martian regolith from Northwest Africa 7034: The important role of Fe oxides.
1031   *Geophys. Res. Lett.* **41**, 8235–8244.
1032 Nuding, D.L., Rivera-Valentin, E.G., Davis, R.D., Gough, R.V., Chevrier, V.F. and Tolbert,
1033   M.A. (2014) Deliquescence and efflorescence of calcium perchlorate: An investigation of
1034   stable aqueous solutions relevant to Mars. *Icarus* **243**, 420-428.
1035 O'Neill, H.S.C. & Mavrogenes, J.A. (2002) The sulfide capacity and the sulfur content at
1036   sulfide saturation of silicate melts at $1400^{o}C$ and 1 bar. *J. Pet.* **43**, 1049-1087.
1037 Oppenheimer, C., Scaillet, B., Martin, R.S. (2011) Sulfur degassing from volcanoes: Source
1038   conditions, surveillance, plume chemistry and earth system impacts. *Rev. Mineral.
1039   Geochem.* **73**, 363–421.
1040 Pavlov, A.A. and Kasting, J.F. (2002) Mass-independent fractionation of sulfur isotopes in
1041   Archean sediments: Strong evidence for an anoxic Archean atmosphere. *Astrobiology* **2**,
1042   27-41.
1043 Planavsky, N.J., Asael, D., Hofmann, A., Reinhard, C.T., Lalonde, S.V., Knudsen, A., Wang,
1044   X., Ossa, F.O., Pecoits, E., Smith, A.J.B., Beukes, N.J., Bekker, A., Johnson, T.M.,
1045   Konhauser, K.O., Lyons, T.W. and Rouxel, O.J. (2014) Evidence for oxygenic
1046   photosynthesis half a billion years before the Great Oxidation Event. *Nature Geosci.* **7**,
1047   283-286.
1048 Robertson, K. and Bish, D. (2011) Stability of phases in the $Mg(ClO_4)_2 \cdot nH_2O$ system and
1049   implications for perchlorate occurrences on Mars. *J. Geophys. Res. – Planet.* **116**, E07006.
1050 Santos, A.R., Agee, C.B., McCubbin, F.M., Shearer, C.K., Burger, P.V., Tartese, R. and
1051   Anand, M. (2015) Petrology of igneous clasts in Northwest Africa 7034: Implications for
1052   the petrologic diversity of the martian crust. *Geochim. Cosmochim. Acta* **157**, 56-85.

Schwenzer, S.P., Bridges, J.C., Wiens, R.C., Conrad, P.G., Kelley, S.P., Leveille, R., Mangold, N., Martín- Torres, J., McAdam, A., Newsom, H., Zorzano, M.P., Rapin, W., Spray, J., Treiman, A.H., Westall, F., Fairén, A.G. and Meslin, P.-Y. (2016) Fluids during diagenesis and sulfate vein formation in sediments at Gale crater, Mars. *Meteorit. Planet. Sci.* **51**, 2175–2202.

Shearer, C.K., Bell, A.S., Herd, C.D.K., Burger, P.V., Provencio, P., Sharp, Z.D. and Papike, J.J. (2019) The Northwest Africa 8159 (NWA 8159) Martian Meteorite Part 2. Spinel-orthopyroxene intergrowths. A record of fO$_2$ and crust-basalt interactions. *Geochim. Cosmochim. Acta* **258**, 242–257.

Sholes, S.F., Smith, M.L., Claire, M.W., Zahnle, K.J. and Catling, D.C. (2017) Anoxic atmospheres on Mars driven by volcanism: Implications for past environments and life. *Icarus* **290**, 46-62.

Sossi, P.A. and O'Neill, H.S.C. (2016) Liquidus temperatures of komatiites and the effect of cooling rate on element partitioning between olivine and komatiitic melt. *Contrib. Min. Pet.* **171**, 49.

Squires, S.W., Grotzinger, J.P., Arvidson, R., Bell III, J.F., Calvin, W., Christensen, P.R., Clark, B.C., Crisp, J.A., Farrand, W.H., Herkenhoff, K.E., Johnson, J.R., Klingelhofer, G., Knoll, A.H., Mclennan, S.M., McSween Jr., H.Y., Morris, R.V., Rice, J.W., Rieder, R. and Soderblom, L.A. (2004) In Situ Evidence for an Ancient Aqueous Environment at Meridiani Planum, Mars. *Science* **306**, 1709-1714.

Stern, J.C., Sutter, B., Jackson, W.A., Navarro-González, R., McKay, C.P., Ming, D.W., Archer, P.D. and Mahaffy, P.R. (2017) The nitrate/(per)chlorate relationship on Mars. *Geophys. Res. Lett.* **44**, 2643–2651.

Stoffler, D., Keil, K. and Scott, E.R.D. (1991) Shock metamorphism of ordinary chondrites. *Geochim. Cosmochim. Acta* **55**, 3845-3867.

Tomkins, A.G., Genge, M.J., Tait, A.W., Alkemade, S.L., Langendam, A.D., Perry, P.V. and Wilson, S.A. (2019) High survivability of micrometeorites on Mars: Sites with enhanced availability of limiting nutrients. *J. Geophys. Res. – Planet.* **124** https://doi.org/10.1029/2019JE006005

Toner, J.D. and Catling, D.C. (2018) Chlorate brines on Mars: Implications for the occurrence of liquid water and deliquescence. *Earth Planet. Sci. Lett.* **497**, 161-168.

Udry, A. and Day, J.M.D. (2018) 1.34 billion-year-old magmatism on Mars evaluated from the co-genetic nakhlite and chassignite meteorites. *Geochim. Cosmochim. Acta* **238**, 292-315.

Ueno, Y., Johnson, M.S., Danielache, S.O., Eskebjergc, C., Pandey, A., and Yoshida, N. (2009) Geological sulfur isotopes indicate elevated OCS in the Archean atmosphere, solving faint young sun paradox. *Proc. Nat. Acad. Sci.* **106**, 14784–14789.

Whitehill, A.R., Jiang, B., Guo, H. and Ono, S. (2015) SO$_2$ photolysis as a source for sulfur mass-independent isotope signatures in stratospehric aerosols. *Atmos. Chem. Phys.* **15**, 1843–1864.

Williams, D.A., Greeley, R., Hauber, E., Gwinner, K. and Neukum, G. (2005) Erosion by flowing Martian lava: New insights for Hecates Tholus from Mars Express and MER data. *J. Geophys. Res. – Planet.* **110**, E05006.

Williams, J.T., Shearer, C.K., Sharp, Z.D., Burger, P.V., McCubbin, F.M., Santos, A.R., Agee, C.B. and McKeegan, K.D. (2016) The chlorine isotopic composition of Martian meteorites 1: Chlorine isotope composition of Martian mantle and crustal reservoirs and their interactions. *Meteorit. Planet. Sci.* **51**, 2092–2110.

Wilson, L. and Head, J.W. (2007) Explosive volcanic eruptions on Mars: Tephra and accretionary lapilli formation, dispersal and recognition in the geologic record. J. Volc. Geotherm. Res. **163**, 83–97.

1103 Wittman, A., Korotev, R.L., Jolliff, B.L., Irving, A.J., Moser, D.E., Barker, I. and Rumble III,
1104   D. (2015) Petrography and composition of Martian regolith breccia meteorite Northwest
1105   Africa 7475. *Meteorit. Planet. Sci.* **50**, 326-352.
1106 Wordsworth, R.D. (2016) The Climate of Early Mars. *Ann. Rev. Earth Planet. Sci.* **44**, 1-31.
1107 Yang, S., Humayun, M., Righter, K., Jefferson, G., Fields, D. and Irving, A.J. (2015)
1108   Siderophile and chalcophile element abundances in shergottites: Implications for Martian
1109   core formation. *Meteorit. Planet. Sci.* **50**, 691-714.
1110 Zahnle, K., Claire, M. and Catling, D. (2006) The loss of mass-independent fractionation in
1111   sulfur due to a Palaeoproterozoic collapse of atmospheric methane. *Geobiology* **4**, 271-
1112   283.

1113
1114
1115

1116 **Figure Captions**

1117

1118 **Figure 1**   A comparison between Δ^{33}S data for Earth and Mars as a function of time.

1119

1120 **Figure 2**   Examples of the distribution and petrography of pyrite in Martian polymict
1121 breccias NWA 8171 (A-C) and NWA 11220 (D). A) A broad region of the meteorite
1122 showing the brecciated texture. The distribution of augite is highlighted in light blue
1123 (microprobe mineral map stacked onto a BSE image). B) An example of a larger pyrite grain,
1124 partially replaced by iron oxides (through weathering on Earth), and showing a small analysis
1125 pit remaining after SIMS work. In bright grey can be seen the abundant fine- to medium-
1126 grained magnetite that occurs throughout the sample (the gold remains after polishing off the
1127 coating used in the SIMS analysis). C) The distribution of fine-grained pyrite is highlighted
1128 in bright yellow in this mineral map – BSE image stack. D) Element map of an impact
1129 spherule showing the distribution of sulfur (red), Ca (green) and Mg (blue). An association
1130 between the distribution of some pyrite and calcite filled fractures is clear. In this case, the
1131 larger fractures in the spherule are likely to be contraction cracks formed during cooling.

1132

1133 **Figure 3**   Examples of the relationships between pyrrhotite and other minerals in
1134 shergottites examined in this study. A) In this reflected light image of NWA 10170 (paired
1135 with NWA 2990), most pyrrhotite grains are attached to iron-titanium oxides, suggesting that
1136 sulfide saturation was driven by extraction of FeO from the silicate liquid. B) Element map
1137 for NWA 10170, showing the commonly coincident relationships between pyrrhotite
1138 (yellow), apatite (light blue) and ilmenite (small red grains). C) An example of the close
1139 association seen between iron titanium oxides and pyrrhotite typically seen in shergottites
1140 (NWA 7297 in this case; reflected light). Very fine exsolutions of pentlandite can be seen in
1141 the pyrrhotite. D) Stacked element map for Los Angeles. Pyrrhotite is in brightest green,
1142 apatite is in dark green, iron titanium oxides are in red, silicates are in blue. Sulfides are
1143 generally associated with FeTi-oxides or late-crystallising apatite.

1144

1145 **Figure 4**   Sulfur isotope data for pyrite in Martian polymict breccia NWA 8171. A) Δ^{33}S
1146 versus δ^{34}S; white circles indicate data for 10 μm spots, red spots indicate 7 μm spots, the
1147 yellow diamond indicates the weighted mean of the 10 μm spots, the green diamond is the
1148 shergottite weighted mean from Franz et al. (2019). B) Δ^{36}S versus δ^{34}S; symbols are the
1149 same as in A. C) Δ^{36}S versus Δ^{33}S, the pink shaded area is the previous Mars meteorite data
1150 including 2σ error bars (from Franz et al., 2014; 2019), and the red-outlined blue square is
1151 the weighted mean error window for our 10 μm spot data, which are overlain. D) Comparison
1152 between the NWA 8171 data (dark blue circles) and those for Archean sulfate (white circles)

1153   on Earth, and sulfides found in sulfate-rich layers (black squares) from Muller et al. (2016).
1154   The green field indicates the experimental results of OCS photolysis under a Xe lamp at $\lambda <$
1155   200 nm (from Lin et al., 2011); there is close agreement between this and the weighted mean
1156   error window for the NWA 8171 data (red outline).
1157

1158   **Figure 5** Δ^{33}S data for Martian meteorites other than NWA 7034 (and pairs). A) Data
1159   for shergottites from this study (blue) and from Franz et al. (2014; 2019) (other shades); the
1160   anomalous shergottites NWA 2290 (and pair NWA5960), Los Angeles, NWA 11300 and
1161   NWA 7635 are indicated. B) Data for the nakhlites from Franz et al. (2014; coloured shapes)
1162   and Dottin et al. (2018; grey shapes), highlighting the three anomalous samples, as well as
1163   the ancient orthopyroxenite ALH84001; the field of all shergottite data is indicated in the
1164   small grey field to highlight the differences in the x and y axes of A and B.
1165

1166   **Figure 6**   Schematic illustration of processes affecting the Δ^{33}S system on Mars (see
1167   text) (modified from an equivalent diagram for the δ^{34}S system in Franz et al., 2017).
1168

**Table 1.** Representative electron microprobe analyses of NWA 8171 pyrites.

ID - spot	Fe	Ni	S	As	Co	Total
A - 1	45.86	0.10	53.65	b.d.l.	0.02	99.64
B - 1	46.57	0.02	53.41	0.00	0.01	100.03
B - 2	44.11	1.75	53.04	b.d.l.	0.04	98.97
B - 3	43.48	2.23	53.19	b.d.l.	0.05	98.97
C - 1	45.67	0.10	52.36	0.01	0.02	98.17
C - 2	44.13	1.33	52.04	0.01	0.01	97.53
C - 3	44.76	1.04	52.15	b.d.l.	0.03	97.99
E - 1	45.65	0.07	53.37	0.00	0.00	99.12
H - 1	45.92	0.04	53.49	0.01	0.01	99.50
I - 1	43.75	1.39	54.02	b.d.l.	0.22	99.39
K - 1	45.78	b.d.l.	53.47	b.d.l.	b.d.l.	99.24
K - 2	44.69	0.82	53.36	0.01	0.02	98.92
L - 1	44.93	0.52	53.55	b.d.l.	b.d.l.	99.02
L - 2	45.52	0.00	53.58	b.d.l.	b.d.l.	99.12
N - 1	42.23	3.23	52.86	b.d.l.	0.02	98.35
O - 2	45.40	0.09	53.17	0.01	0.00	98.70
P - 1	45.72	0.17	53.63	0.00	b.d.l.	99.54
Q - 2	44.77	0.46	53.53	0.01	0.06	98.85

All data in wt. %.

Table 2. Sulfur isotope data for samples analysed in this study.

Sample	Spot ∝m	$d^{33}S$	2s	$d^{34}S$	2s	$d^{36}S$	2s	$D^{33}S$	2s	$D^{36}S$	2s
NWA 7320	20	-0.22	0.13	-0.43	0.23	-1.35	0.72	-0.01	0.12	-0.53	0.66
NWA 7320	20	-0.20	0.13	-0.38	0.24	-1.39	0.73	0.00	0.12	-0.66	0.68
NWA 7397	20	-0.03	0.13	0.054	0.22	0.40	0.72	-0.06	0.11	0.30	0.65
NWA 7397	20	-0.12	0.14	-0.11	0.23	-0.48	0.76	-0.07	0.13	-0.28	0.72
NWA 7397	20	-0.40	0.16	-0.77	0.28	-2.51	0.84	0.00	0.17	-1.04	0.84
NWA 7397	20	0.02	0.13	0.15	0.23	0.13	0.71	-0.05	0.11	-0.17	0.65
NWA 7397	20	0.09	0.14	0.07	0.24	-0.21	0.76	0.05	0.13	-0.35	0.71
NWA 7397	20	0.09	0.14	0.24	0.23	-0.02	0.72	-0.04	0.12	-0.48	0.67
NWA 7397	20	0.24	0.14	0.59	0.24	0.63	0.73	-0.06	0.13	-0.50	0.68
NWA 7397	20	0.16	0.14	0.11	0.24	-0.17	0.79	0.11	0.14	-0.37	0.75
NWA 7397	20	-0.40	0.16	-0.77	0.28	-2.51	0.84	0.00	0.17	-1.04	0.84
NWA 7397	20	0.02	0.13	0.15	0.23	0.13	0.71	-0.05	0.11	-0.17	0.65
NWA 8656	20	-0.46	0.21	-0.88	0.33	-1.29	0.97	0.00	0.15	0.39	0.90
NWA 8656	20	-0.37	0.21	-0.84	0.34	-2.34	0.97	0.06	0.15	-0.74	0.91
NWA 8656	20	-0.39	0.20	-0.68	0.33	-0.85	0.98	-0.04	0.14	0.46	0.90
NWA 8656	20	-0.59	0.21	-1.20	0.35	-2.32	1.05	0.03	0.16	-0.03	1.01
NWA 8656	20	-0.47	0.20	-0.91	0.31	-1.54	0.97	0.00	0.12	0.19	0.88
NWA 8656	20	-0.20	0.20	-0.42	0.32	0.23	0.94	0.02	0.13	1.03	0.84
NWA 8656	20	-0.36	0.20	-0.85	0.32	-0.82	0.90	0.08	0.13	0.81	0.81
NWA 8656	20	-0.29	0.20	-0.40	0.31	-0.81	0.92	-0.09	0.13	-0.04	0.82
NWA 8656	20	-0.42	0.21	-0.80	0.32	-1.25	0.96	0.00	0.14	0.28	0.87
NWA 8656	20	-0.85	0.22	-1.68	0.35	-2.51	0.97	0.02	0.17	0.70	0.93
NWA 8656	20	-0.70	0.21	-1.29	0.34	-2.84	0.96	-0.04	0.15	-0.37	0.90
NWA 8656	20	-0.55	0.22	-0.96	0.35	-0.82	0.98	-0.06	0.17	1.00	0.94
NWA 8716	20	-0.04	0.21	0.02	0.34	0.71	0.98	-0.05	0.16	0.67	0.91
NWA 8171	10	-1.06	0.22	-1.62	0.37	-4.18	0.94	-0.22	0.28	-1.09	1.21
NWA 8171	10	-0.75	0.20	-1.09	0.37	-2.60	0.98	-0.19	0.26	-0.52	1.23
NWA 8171	10	-1.45	0.24	-2.34	0.36	-4.59	1.09	-0.24	0.29	-0.13	1.32
NWA 8171	10	-0.94	0.20	-1.80	0.36	-4.17	0.88	-0.02	0.26	-0.75	1.15
NWA 8171	10	-1.55	0.20	-2.99	0.38	-6.07	0.94	-0.01	0.27	-0.36	1.22
NWA 8171	10	-0.59	0.21	-0.98	0.38	-2.50	0.95	-0.09	0.27	-0.63	1.23
NWA 8171	10	-0.81	0.19	-1.14	0.33	-2.92	0.90	-0.22	0.24	-0.75	1.13
NWA 8171	10	-2.84	0.16	-5.21	0.31	-11.21	1.07	-0.15	0.21	-1.27	1.26
NWA 8171	10	-0.51	0.19	-0.70	0.37	-2.03	0.94	-0.15	0.25	-0.69	1.21
NWA 8171	7	0.51	0.21	1.02	0.30	2.34	0.85	-0.01	0.19	0.40	0.92
NWA 8171	7	-0.16	0.32	-0.05	0.54	-0.48	1.18	-0.13	0.38	-0.38	1.50
NWA 8171	7	-0.45	0.26	-0.32	0.39	-0.24	0.97	-0.29	0.27	0.36	1.14
NWA 8171	7	-3.07	0.22	-6.09	0.30	-12.37	0.94	0.07	0.20	-0.77	1.01
NWA 8171	7	-0.14	0.25	0.00	0.38	-1.45	0.95	-0.14	0.26	-1.46	1.11
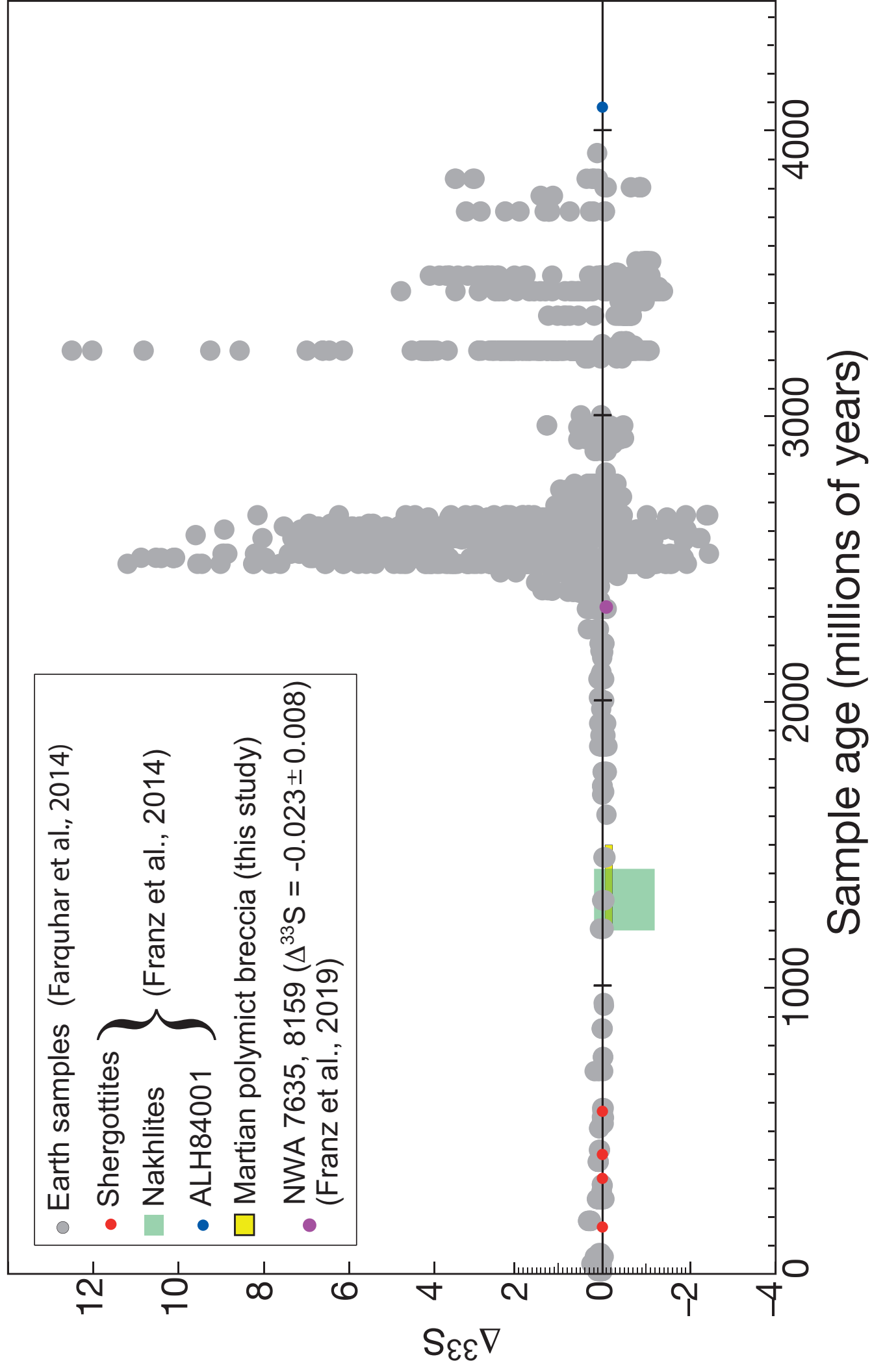
Figure

Figure

Electronic Annex
Click here to download Electronic Annex: research data.xlsx

The authors declare no competing interest.